

# Materials Advances

Accepted Manuscript

This article can be cited before page numbers have been issued, to do this please use: S. M. Tikhanova, M. P. Volkov, I. V. Burianenko, V. Semenov, Z. Orazov, V. Romanovski, V. I. Popkov and N. A. Lomanova, *Mater. Adv.*, 2026, DOI: 10.1039/D6MA00153J.



This is an Accepted Manuscript, which has been through the Royal Society of Chemistry peer review process and has been accepted for publication.

Accepted Manuscripts are published online shortly after acceptance, before technical editing, formatting and proof reading. Using this free service, authors can make their results available to the community, in citable form, before we publish the edited article. We will replace this Accepted Manuscript with the edited and formatted Advance Article as soon as it is available.

You can find more information about Accepted Manuscripts in the [Information for Authors](#).

Please note that technical editing may introduce minor changes to the text and/or graphics, which may alter content. The journal's standard [Terms & Conditions](#) and the [Ethical guidelines](#) still apply. In no event shall the Royal Society of Chemistry be held responsible for any errors or omissions in this Accepted Manuscript or any consequences arising from the use of any information it contains.

1 **Synthesis of a novel visible light-driven and magnetically separable photocatalyst based**  
2 **on BiFeO<sub>3</sub>-YFeO<sub>3</sub> type II heterojunction**

3  
4 **Sofia M. Tikhanova**<sup>1</sup>, **Mikhail P. Volkov**<sup>2</sup>, **Ivan V. Buryanenko**<sup>3</sup>, **Valentin G. Semenov**  
5 **<sup>3,4</sup>, Zhandos Orazov**<sup>5</sup>, **Valentin Romanovski**<sup>6,\*</sup>, **Vadim I. Popkov**<sup>1</sup>, **Natalia A.**  
6 **Lomanova**<sup>7,\*</sup>

7 <sup>1</sup> Hydrogen Energy Laboratory, Ioffe Institute, St. Petersburg 194021, Russia

8 <sup>2</sup> Laboratory of Kinetic Phenomena in Solids at Low Temperatures, Ioffe Institute, St.  
9 Petersburg 194021, Russia

10 <sup>3</sup> RITVERC JSC, St. Petersburg 194223, Russia

11 <sup>4</sup> Mössbauer Spectroscopy Laboratory, Institute for Analytical Instrumentation of RAS, St.  
12 Petersburg 198095, Russia

13 <sup>5</sup> Center of Physical Chemical Methods of Research and Analysis, Al-Farabi Kazakh National  
14 University, Almaty 050040, Kazakhstan

15 <sup>6</sup> Department of Materials Science and Engineering, University of Virginia, Charlottesville  
16 22904, USA

17 <sup>7</sup> Laboratory of New Inorganic Materials, Ioffe Institute, St. Petersburg 194021, Russia

18  
19 \* Corresponding author e-mail:

20 Valentin Romanovski: [rvd9ar@virginia.edu](mailto:rvd9ar@virginia.edu)

21 Natalia A. Lomanova: [natus@mail.ioffe.ru](mailto:natus@mail.ioffe.ru)



22 **Abstract.** Nanocomposites based on the  $\text{BiFeO}_3\text{-YFeO}_3$  system with different phase ratios  
23 have been synthesized via the solution combustion route. The nominal compositions were set  
24 as  $x\text{BiFeO}_3\text{-(1-x)YFeO}_3$  (where  $x = 0.1, 0.3, 0.4, 0.5, 0.6, 0.7,$  and  $0.9$ ), labeled from BYFO-  
25 01 to BYFO-09. Glycine was used as a reducing agent for the combustion reaction. The average  
26 crystallite size of the obtained materials was in the range of 25–90 nm. A study of the magnetic  
27 characteristics and photocatalytic activity of the samples showed that variations in their phase  
28 composition significantly enhance both total magnetization and the photodegradation of  
29 Rhodamine B dye. All samples exhibit magnetic ordering at room temperature and increased  
30 magnetization compared to pure bismuth and yttrium orthoferrites. It was found that the  
31 BYFO-04 nanocomposite possesses enhanced photocatalytic activity, which was attributed to  
32 the approximately 1:1 orthoferrite phase ratio. The BYFO-0.5 and BYFO-0.7 nanocomposites  
33 showed an improved magnetic response, with specific and saturation magnetization values of  
34 approximately 8 emu/g at a field of 4 kOe. The increased magnetization of these samples was  
35 explained by their phase composition, which can be technologically controlled. The discovered  
36 properties of the synthesized materials are promising for the effective separation of  
37 photocatalysts from the reaction medium. The BYFO-0.4 sample photodegraded about 40% of  
38 the rhodamine B dye and 80% of methyl violet within 180 minutes of irradiation with visible  
39 light. The easy synthesis method, combined with magnetic and photocatalytic responses and  
40 environmentally benign iron sources, makes  $\text{BiFeO}_3\text{-YFeO}_3$  nanocomposites promising  
41 materials for photocatalytic systems and memory recording applications.

42  
43 **Keywords:** orthoferrites, nanoparticles, combustion method, magnetic properties,  
44 photocatalytic activity

View Article Online  
DOI: 10.1039/D6MA00153J



## 45 1. Introduction

46 Recent research of multiferroics has focused on orthoferrites  $A\text{FeO}_3$  ( $A = \text{Bi}, \text{Y}$ ) due to  
47 their promising magnetic and electrical characteristics, and photocatalytic activity [1–16]. At  
48 present, orthoferrites  $\text{BiFeO}_3$  and  $\text{YFeO}_3$  are used as materials for magnetic storage devices  
49 [1,2,4,8,9], gas sensors [2,4], photocatalytic systems [3,5–7,9,10,17,18], etc.

50 Bismuth orthoferrite ( $\text{BiFeO}_3$ ) is popular magnetoelectric material because it exhibits  
51 multiferroic properties at room temperature and above it.  $\text{BiFeO}_3$  has the Neel temperature of  
52  $T_N \approx 360^\circ\text{C}$  and Curie temperature of  $T_C \approx 830^\circ\text{C}$  [9]. Below  $T_C$ , bismuth orthoferrite exists in the  
53 form of an  $\alpha$ -phase with a rhombohedral perovskite-like crystal structure ( $R3c$  space group)  
54 [19]. This material combines the properties of ferroelasticity, antiferromagnetism and  
55 ferroelectricity [2,9]. The magnetic nature of  $\text{BiFeO}_3$  is described as  $G$ -type antiferromagnetic  
56 order of  $\text{Fe}^{3+}$  ions with a space-modulated cycloid spin structure having a period  $\lambda_c = 62 \pm 2$  nm  
57 [2].  $\text{BiFeO}_3$  nanocrystals exhibit weak ferromagnetism arising from the canting of the  
58 antiferromagnetic Fe sublattices and the appearance of the Dzyaloshinskii-Moriya effect  
59 [9,13].

60 Yttrium orthoferrite ( $\text{YFeO}_3$ ) is an attractive material due to its excellent magneto-  
61 optical properties and extraordinary domain wall motion [20]. In addition, the coupling of  
62 magnetic and ferroelectric ordering in  $\text{YFeO}_3$  makes it us to consider this compound as a  
63 promising multiferroic [21].

64 One of the ways to improve the performance of the orthoferrites is to create  
65 nanocomposite materials, i.e., of systems that include two or more components [13–16,22–29].  
66 Recently, the development of nanocomposites has become a key area in the research of  
67 advanced multiferroics. Of particular interest are materials with magnetic order at room  
68 temperature. Moreover, nanocomposites can have improved photocatalytic activity due to the  
69 formation of new active centers. The synthesis and properties of nanocomposite materials  
70 based on bismuth and yttrium orthoferrites with different phase compositions have been  
71 described in [14,24,27–31]. Most researchers indicate that composite materials based on  
72 orthoferrites have improved magnetic and photocatalytic responses and can be synthesized  
73 using «soft» chemical methods. Nanomaterials based on bismuth and yttrium orthoferrites are  
74 photocatalysts whose performance can be enhanced by doping [22]. These materials have  
75 proven to be very useful for the degradation of dyes under visible light irradiation among other  
76 photocatalysts.



77 Solution combustion synthesis is an effective method for the synthesis of oxide  
78 nanoparticles and nanocomposites since it is an energy- and time-saving method that does not  
79 require expensive equipment [13,14,32–40]. Currently, this technique is actively used for the  
80 synthesis of orthoferrites (e.g. [3,13,14,27,30,32,39–46]). Such conditions of synthesis as the  
81 type of organic fuel and the ratio of fuel to oxidizer strongly affect the formation and properties  
82 of oxide nanomaterials [39,41,42,45,46], including BiFeO<sub>3</sub> and YFeO<sub>3</sub>.

83 The available data on the properties of the Bi<sub>1-x</sub>Y<sub>x</sub>FeO<sub>3</sub>/Y<sub>1-x</sub>Bi<sub>x</sub>FeO<sub>3</sub> materials are  
84 fragmentary and apply only to some compositions. Materials based on the BiFeO<sub>3</sub>-YFeO<sub>3</sub>  
85 system are presented in the literature, mainly as solid solutions of the Bi<sub>1-x</sub>Y<sub>x</sub>FeO<sub>3</sub>/Y<sub>1-x</sub>Bi<sub>x</sub>FeO<sub>3</sub>  
86 type with a narrow range of  $x < 0.3$  [5,47–51]. It is noted that with increasing doping, the  
87 magnetic response and photocatalytic activity of the Bi<sub>1-x</sub>Y<sub>x</sub>FeO<sub>3</sub> materials improve [47,48,51].  
88 The successful synthesis of phases in the range  $0 < x < 1$  has apparently been reported only in  
89 [52], but the functional properties of most samples have not been studied. There are no  
90 publications devoted to the magnetic study of nanocomposites BiFeO<sub>3</sub>-YFeO<sub>3</sub>. The increased  
91 photocatalytic activity of Y-doped nanocomposites is reported in [5,51]. Based on the data on  
92 doped materials and pure orthoferrites, we hypothesize that the BiFeO<sub>3</sub>-YFeO<sub>3</sub> system may  
93 yield new materials with magnetic order at room temperature and enhanced magnetic and  
94 photocatalytic responses.

95 The aim of this study was to synthesize BiFeO<sub>3</sub>-YFeO<sub>3</sub> nanocomposites via glycine-  
96 nitrate combustion synthesis and analyze the obtained materials in terms of their magnetic and  
97 photocatalytic applications.

## 98 2. Materials and methods

### 99 2.1 Materials and reagents

100 Nanocomposites based on the BiFeO<sub>3</sub>-YFeO<sub>3</sub> system were synthesized via the glycine-  
101 nitrate combustion method. Crystallohydrates of metal nitrates Bi(NO<sub>3</sub>)<sub>3</sub>·5H<sub>2</sub>O,  
102 Y(NO<sub>3</sub>)<sub>3</sub>·6H<sub>2</sub>O, Fe(NO<sub>3</sub>)<sub>3</sub>·9H<sub>2</sub>O, and glycine C<sub>2</sub>H<sub>5</sub>NO<sub>2</sub> of p.a. purity grade were used as initial  
103 reagents. Metal nitrates were mixed in a proportion corresponding to the nominal compositions  
104 of  $x\text{BiFeO}_3-(1-x)\text{YFeO}_3$  with  $x = 0.1, 0.3, 0.4, 0.5, 0.6, 0.7,$  and  $0.9$ .

### 105 2.2 Materials synthesis procedure

106 The amount of glycine used as organic fuel corresponded to a glycine-nitrate (*G/N*)  
107 ratio of 0.55. Metal nitrates and glycine were dissolved in 100 ml of 1M HNO<sub>3</sub> aqueous solution  
108 with constant stirring and heating. The obtained solutions were heated until the water  
109 evaporated and the reaction mixtures spontaneously combusted, resulting in the formation of  
110



111 brown powders. The combustion products were sequentially calcined in the temperature range  
112 of 350–750 °C for 1 hour at each stage. View Article Online  
DOI: 10.1039/L5MA00153J

113 Thus, reference samples of BiFeO<sub>3</sub> (BFO) and YFeO<sub>3</sub> (YFO) were synthesized, as well  
114 as a series of  $x\text{BiFeO}_3-(1-x)\text{YFeO}_3$  ( $x = 0.1, 0.3, 0.4, 0.5, 0.6, 0.7, \text{ and } 0.9$ ) samples. The mixed  
115 Bi-Y orthoferrite samples were named according to Y content - from BYFO-01 to BYFO-09.  
116 The prepared samples were characterized by following physicochemical methods.

### 117 *2.3 Materials characterization*

118 The morphology of the samples was studied by scanning electron microscopy (FEI  
119 Quanta 200 SEM with the EDAX attachment), and the elemental composition of the samples  
120 was checked by energy dispersive X-ray analysis.

121 The powder X-ray diffraction (XRD) patterns of the samples was measured at room  
122 temperature by using CuK $\alpha$  X-ray source (Rigaku SmartLab 3) for the Bragg angle ( $2\theta$ ) range  
123 of 20-70°. To calculate unit cell parameters, the SmartLab software package was used.

124 A Wissel spectrometer with a <sup>57</sup>Co source in a rhodium matrix was used for the  
125 Mössbauer examination of the sample at room temperature (isomeric shifts  $IS$  are given relative  
126 to the  $IS$  of  $\alpha$ -Fe). Spectra fittings were made with the Mossfit software.

127 Magnetic measurements were performed with the Physical Properties Materials System  
128 (PPMS) provided by the Quantum Design using vibrating sample magnetometer option. At  
129 room temperature, the dependences of the specific magnetization  $M$  on the field  $H$  were  
130 studied. For single-phase samples, they were measured up to 40 kOe, for nanocomposites - up  
131 to 4 kOe.

132 The photocatalytic activity was assessed by photodegradation of the Rhodamine B dye  
133 (RdB) under the action of visible light. 30 mg of the photocatalyst was added to a solution of  
134 10 mg/L RdB, and the resulting mixture was treated with ultrasound for 3 min to achieve  
135 maximum dispersion. To increase the photocatalytic activity (photo-Fenton-like mode), 1 mL  
136 of 3% H<sub>2</sub>O<sub>2</sub> was added. Before irradiation, the mixture was stirred for 60 minutes without light,  
137 and then the degree of dye adsorption and desorption on the catalyst surface was determined.

138 The visible light source was a 300 W Osram Vita-lux lamp with a UV filter. The  
139 irradiation intensity in all experiments was 15 mW/cm<sup>2</sup>. The probes were taken every 30  
140 minutes, and the powders were separated from them by a centrifuge. The rate of photocatalytic  
141 degradation of RhB was estimated from the change with time in the absorption spectrum of the  
142 solutions. The maximum absorption of RhB is at a wavelength of 550 nm. The absorption  
143 spectrum of the solutions was determined on an EMC-11-UV spectrophotometer.



144 The light absorption ability of the samples was investigated by diffuse reflectance  
145 spectra (DRS) in the UV-visible region recorded at room temperature in the range of 400–800  
146 nm using an AvaSphere-30-Refl integrating sphere.

147 The band gap energy ( $E_g$ ) was calculated from the plot of the Kubelka-Munk function:

$$F(R) = \frac{(1 - R)^n}{2R} = \frac{K}{S} \quad (1)$$

148 where  $K$  is the molar absorption coefficient,  $S$  is the scattering factor, and  $R$  is the reflectance  
149 of the material. The  $n$  value is determined by the nature of the sample ( $n = 2$  for direct allowed  
150 transitions and  $n = 1/2$  for indirect allowed transitions).

151 For statistical analysis of the entire volume of the obtained data, the Pearson matrix was  
152 used. For the machine analysis of the dependence of the functional characteristics of BiFeO<sub>3</sub>–  
153 YFeO<sub>3</sub> nanocomposites on the composition, variables reflecting the content of bismuth and  
154 yttrium were used. The experimentally measured parameters characterizing the photocatalytic  
155 properties (reaction rate constant  $k$ , min<sup>-1</sup>; degree of adsorption; time to reach 10% degradation  
156  $t_{10\%}$ , min; removal efficiency RE; final dye concentration  $C_{\text{final}}$ , g/L; amount of reacted  
157 substance  $C_{\text{reacted}}$ , g/L) and magnetic parameters (excess iron  $Fe_{\text{excess}}$ ; magnetization  $M$ , emu/g  
158 at 4 kOe; residual magnetization  $M_r$ , emu/g; coercive force  $H_c$ , kOe) were used as response  
159 variables. Eight models were used to describe the relationships between composition and  
160 functional properties: a classical polynomial regression model and seven machine learning  
161 algorithms: CatBoost, Gaussian process regression (GPR), ElasticNet-poly, ElasticNet,  
162 eXGBoost, eLasso, and a support vector machine (SVR). Model evaluation was performed  
163 using the coefficient of determination.

### 164 3. Results and discussion

#### 165 3.1. Energy-dispersive X-ray (EDX) spectroscopy and scanning electron microscopy 166 (SEM)

167 The morphology and elemental composition were investigated by SEM/EDXS. The  
168 EDX spectra of two typical samples (BYFO-03-09) are shown in Fig. S1 and indicate that the  
169 prepared materials contain only the desired Bi, Y, Fe, and O elements. Elemental analysis of  
170 BFO and YFO samples showed that, the metals ratio in which were 1:1, i.e., it corresponded to  
171 the BiFeO<sub>3</sub> and YFeO<sub>3</sub> stoichiometry (see Table S1).

172 Additionally, samples BFO, BYFO-01, and BYFO-09 have average element ratios of  
173 Bi/Y/Fe that are fairly close to the nominal values. An excess of iron (d) was detected in the  
174



175 BYFO-03-07 samples that had the highest concentration of iron-containing impurities (Fig. S1) View Article Online  
DOI: 10.1039/D6MA00153J  
176 (see Table S2).

177 Fig. S2 presents SEM images of the samples. It can be seen that the BFO morphology  
178 is a network of sintered grains with a rhombic-like shape. With changes in phase and elemental  
179 composition of the materials, the grain morphology becomes less ordered. Doped samples have  
180 porous grains with cavities that were formed due to the rapid release of the combustion gases.

181 The grain size was determined by measuring a substantial number of grains in SEM  
182 images. Y-doping leads to a decrease in particle size and a change in morphology. Thus,  
183 samples BYFO-01-04 consist of porous agglomerates of elongated particles, and their  
184 micrographs indicate that the grain size is reduced three times (Table S1).

185 Yttrium ions are less mobile than  $\text{Bi}^{3+}$  ions, and they slow down the solid-state reaction  
186 during sequential heat treatment of samples, preventing grain growth. The synthesis  
187 temperature of these materials was  $750\text{ }^{\circ}\text{C}$ , compared to  $550\text{ }^{\circ}\text{C}$  previously used for the glycine-  
188 nitrate synthesis of pure  $\text{BiFeO}_3$  [46].

189 Many dopants were reported to suppress grain growth, and other authors have also  
190 assumed that doped  $\text{BiFeO}_3$  may require slightly higher sintering temperatures. A similar  
191 particle morphology was observed in [48], with yttrium doping up to 10%. With a subsequent  
192 increase in yttrium content, the particles become flake-shaped and aggregate into disordered  
193 porous particles, the size of which increases with increasing Y (see Fig. 2, Table 2, samples  
194 BYFO-06-09). The pure YFO sample consists of highly aggregated flake-like particles with an  
195 average grain size of  $2.1\text{ }\mu\text{m}$ , which is the maximum for all series of samples.

### 197 3.2. Powder X-ray diffraction (PXRD)

198 The selection of nanocomposite synthesis regimes was based on previously data on pure  
199  $\text{BiFeO}_3$  with enhanced magnetic and photocatalytic characteristics [37]. The samples were  
200 sequentially heat-treated in the range of  $350\text{--}750\text{ }^{\circ}\text{C}$ . After annealing at  $750\text{ }^{\circ}\text{C}$ , the samples  
201 contained minimal amounts of impurity phases.

202 Fig. 1 shows the XRD patterns of the samples after final heat treatment at  $750\text{ }^{\circ}\text{C}$ . The  
203 observed X-ray reflections of the main phase in the BFO and BYFO-01 samples correspond to  
204 bismuth orthoferrite  $\text{BiFeO}_3$ . The peaks in these PXRD patterns can be indexed to the  
205 rhombohedral, distorted perovskite-like structure (PDF #14-181). In the BYFO-09 and YFO  
206 samples, the main phase is perovskite-like yttrium orthoferrite. The reflections in their PXRD  
207 patterns correspond to orthorhombic phase  $\text{YFeO}_3$  (PDF #8-150). The crystallite sizes of the  
208 main phases in these samples are given in Table 1. Obtained results are consistent with other



works [5,51], and indicate the formation of  $\text{Bi}_{1-x}\text{Y}_x\text{FeO}_3/\text{Y}_{1-x}\text{Bi}_x\text{FeO}_3$  solid solutions at values of  $x \leq 0.1$ .

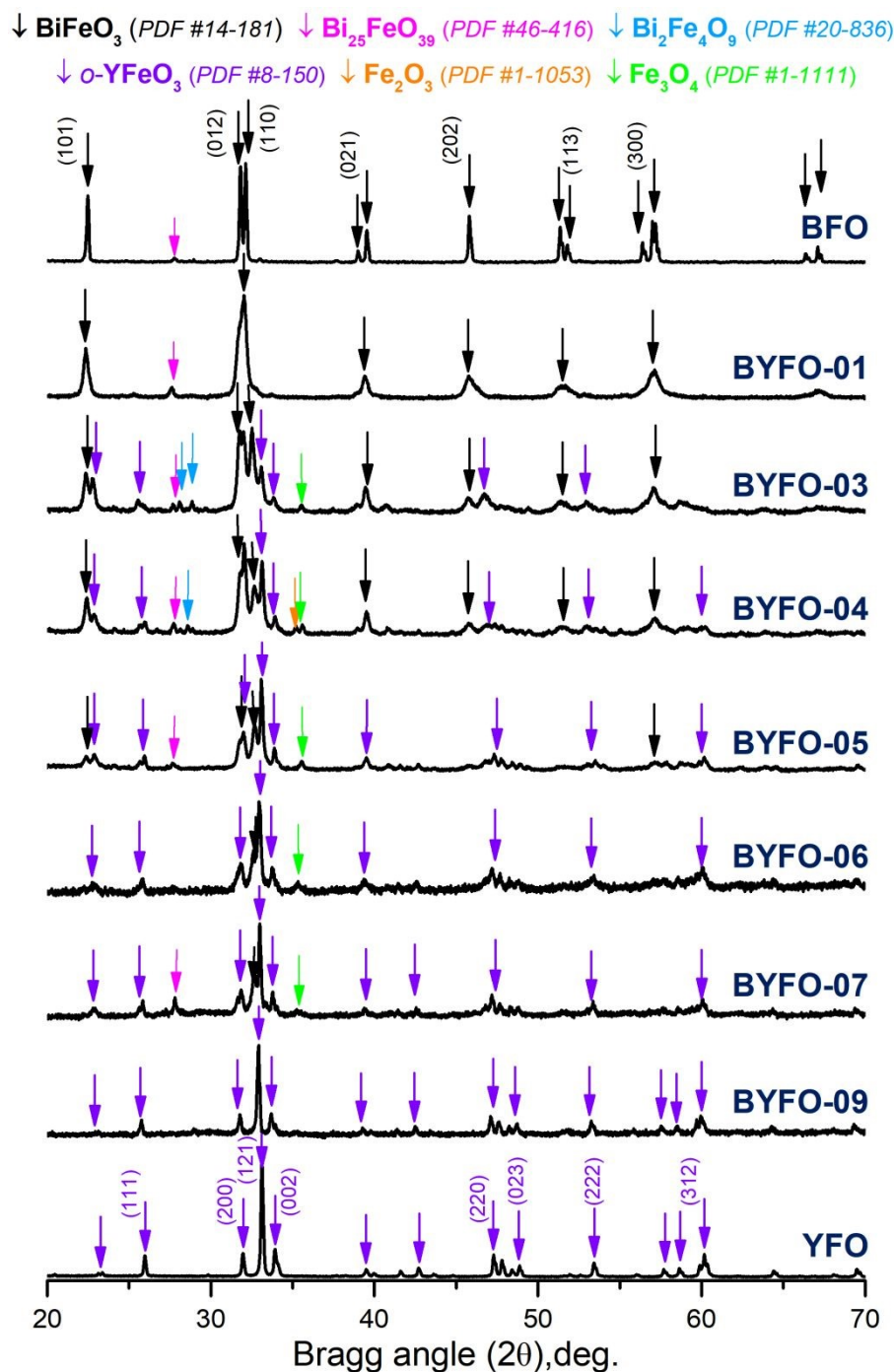


**Fig. 1.** PXRD patterns of the BFO-YFO samples after heat treatment at 750 °C.

211

212

213

214

215

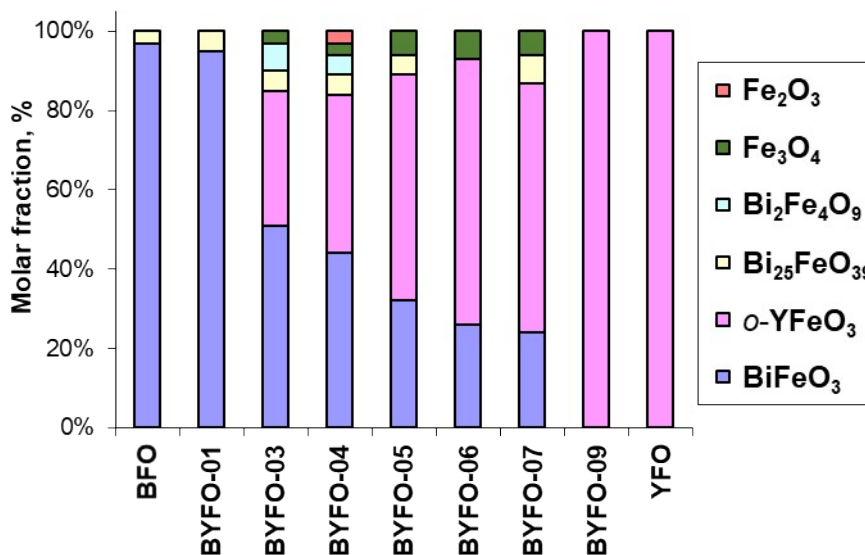
216

217

The observed X-ray reflections for the BYFO-03-07 samples correspond to a mixture of the main phases,  $\text{BiFeO}_3$  and  $\text{YFeO}_3$ . Along with these phases, almost all samples contain traces of bismuth ferrites with sillenite-like ( $\text{Bi}_{25}\text{FeO}_{39}$ ) and mullite-like ( $\text{Bi}_2\text{Fe}_4\text{O}_9$ ) structures. These composite materials likely contain small amounts of iron oxides. Specifically, the



218 BYFO-03-07 samples contain a small amount of magnetite  $\text{Fe}_3\text{O}_4$ , which exhibits a weak  
 219 characteristic (311) peak around  $35.4^\circ$ . Detailed information on the phase composition of the  
 220 synthesized samples is presented in Fig. 2.



221  
 222 **Fig. 2.** Phase composition of the BFO-YFO samples  
 223

224 The causes of the formation of composites in the intermediate region of yttrium  
 225 concentration may be the following: Firstly, the bismuth content decreases with increasing  
 226 yttrium content in these materials, and besides,  $\text{Bi}_2\text{O}_3$  evaporation begins above  $700^\circ\text{C}$ .  
 227 Therefore, an excess amount of bismuth nitrate in the initial composition might be required to  
 228 avoid the formation of secondary phases.

229 According to [47], the appearance of these by-products could also be caused by lattice  
 230 strain resulting from the ionic size mismatch between the host and substituent cations. The  
 231 effective ionic radius of  $\text{Y}^{3+}$  ( $1.02 \text{ \AA}$  for coordination number  $CN = 8$ ) is smaller than that of  
 232  $\text{Bi}^{3+}$  ( $1.17 \text{ \AA}$  in the same coordination) [53]. To further clarify the phase composition of the  
 233 synthesized materials, the data from  $^{57}\text{Fe}$  Mössbauer spectroscopy data are presented in the  
 234 following subsection.

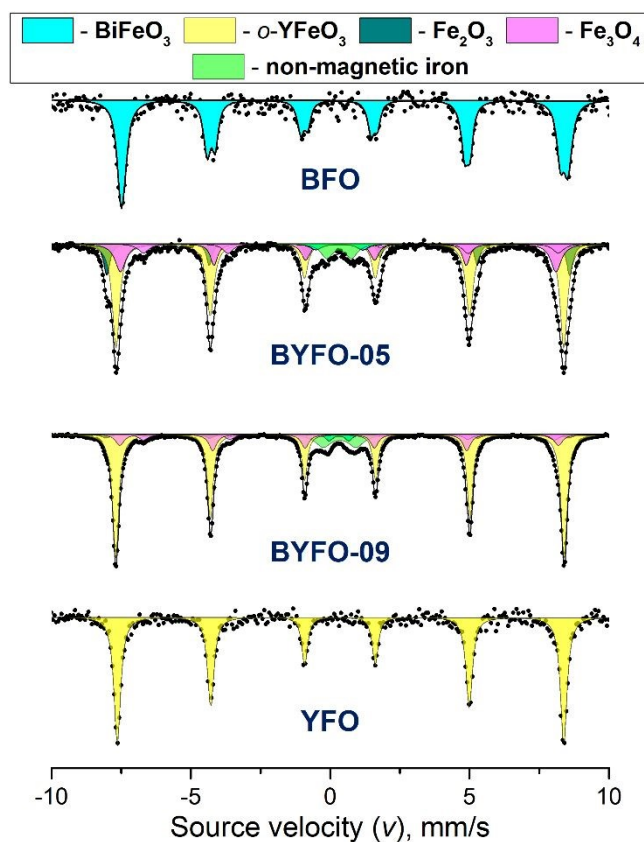
235 The average crystallite sizes ( $d$ ) of the synthesized particles were estimated from the  
 236 XRD patterns using the Scherrer equation and are given in Table 1. The calculation was  
 237 performed using the most intense reflections of the primary phases,  $\text{BiFeO}_3$  (012/110) and  $o\text{-YFeO}_3$   
 238 ( $121/002$ ). The average crystallite sizes vary depending on the phase composition,  
 239 which may be due to spatial limitations on their growth. The estimated  $d$  values for the  
 240 orthoferrites  $\text{BiFeO}_3$  and  $\text{YFeO}_3$  are 87 nm and 71 nm, respectively (see Table S1). The



241 crystallite size in the doped materials is smaller than in the pure orthoferrites' samples, as can  
 242 be seen for samples BYFO-01 and BYFO-09. In addition, we did not observe significant  
 243 differences in the crystallite size for the BYFO-01 and BYFO-09 samples or the composite  
 244 samples. The lack of a clear dependence of  $d$  value on the sample composition may be caused  
 245 by the overlap of diffraction lines from the main phases, making their precise separation  
 246 difficult.

### 248 3.3. $^{57}\text{Fe}$ Mössbauer spectroscopy

249  $^{57}\text{Fe}$  Mössbauer spectra of the BFO, BYFO-05, BYFO-09, and YFO samples are shown  
 250 in Fig. 3. As determined from the spectra, the synthesized materials contain magnetically  
 251 ordered phases at room temperature. The spectra of the BFO and YFO samples consist of  
 252 sextets, with parameters characterizing the state of iron ions in the magnetically ordered  
 253  $\text{BiFeO}_3$  and  $\text{YFeO}_3$  phases, respectively [42,45,46]. The spectra of composite samples BYFO-  
 254 05 and BYFO-09 represent a superposition of sextets and doublets. The parameters of the two  
 255 doublets in these spectra correspond to octahedrally coordinated  $\text{Fe}^{3+}$  ions in  
 256 superparamagnetic  $\text{BiFeO}_3$  particles and paramagnetic (or non-magnetic) iron species.



258

259 **Fig. 3.**  $^{57}\text{Fe}$  Mössbauer RT-spectra of the BFO, BYFO-05, BYFO-09, and YFO samples.



260

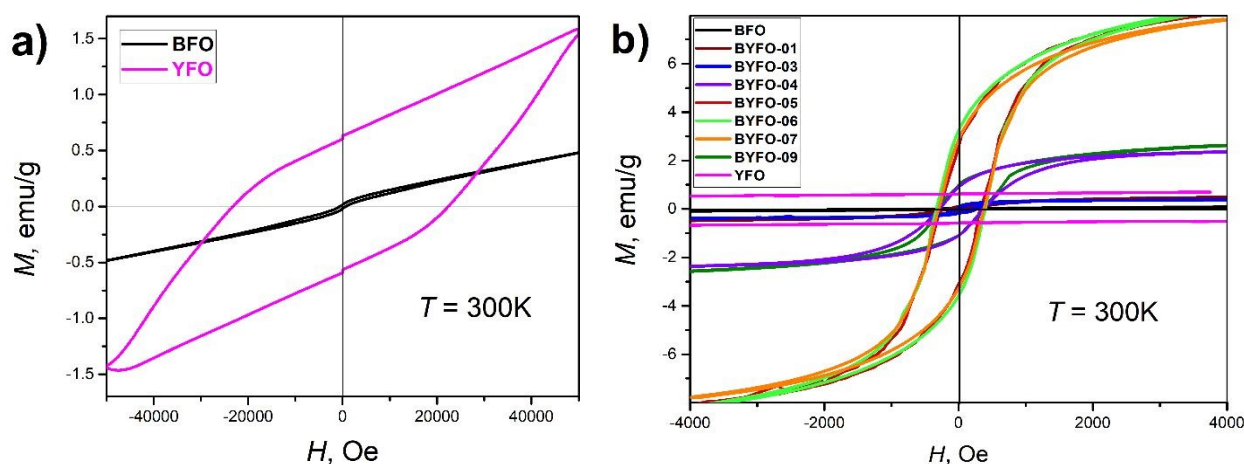
261 Comparing the results of the XRD and  $^{57}\text{Fe}$  Mössbauer spectroscopy, it is clear that the  
 262 BYFO-04-09 samples contain several iron-containing phases: orthoferrites  $\text{BiFeO}_3$  and  $\text{YFeO}_3$ ,  
 263  $\text{Fe}_2\text{O}_3$  and  $\text{Fe}_3\text{O}_4$  iron oxides, and a phase with non-magnetic iron. In the BYFO-05 and BYFO-  
 264 09 samples, the majority of the iron atoms can be attributed to the magnetically ordered  $\text{YFeO}_3$   
 265 phase, the content of which is higher in the BYFO-09 sample. Table S3 summarizes the spectral  
 266 parameters of the primary phases in comparison with the literature data.

267

### 268 3.4. PPMS vibrational magnetometry

269 The magnetization ( $M$ ) of the orthoferrite samples as a function of the magnetic field  
 270 ( $H$ ) at 300K is shown in Fig. 4a . The hysteresis loops were recorded at room temperature (RT).  
 271 The presence of these hysteresis loops indicates that both BFO and YFO materials exhibit  
 272 magnetic ordering at RT.

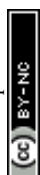
273



274 **Fig. 4.** RT magnetic hysteresis loops of pure BFO, YFO (a) and BYFO (b) samples.

275

276 Nanocrystalline  $\text{BiFeO}_3$  has a narrow hysteresis loop and non-zero magnetization. The  
 277 non-saturating behavior of the loop implies the presence of competing antiferromagnetic  
 278 interactions in  $\text{BiFeO}_3$  nanoparticles that have an ordered AFM core and uncompensated spins  
 279 at the surface of nanocrystals [54]. Surface magnetization contributes to the total magnetic  
 280 response of  $\text{BiFeO}_3$  nanoparticles, and such materials can exhibit significantly higher  
 281 magnetization compared to bulk samples [9]. In our case, the average size of  $\text{BiFeO}_3$  crystallites  
 282 is slightly larger than the period of the spin cycloid  $d > \lambda_c$  (see Table S1), as a result of which  
 283 this sample exhibits only a small magnetic response, which is consistent with other studies  
 284 [4,9,39].



285 The YFO sample displays magnetic properties typical of nanocrystalline yttrium  
286 orthoferrite obtained by glycine-nitrate combustion. At RT, weak ferromagnetic behavior is  
287 observed, resulting from spin canting in the antiferromagnetically ordered  $\text{Fe}^{3+}$  sublattice,  
288 which is caused by Dzyaloshinskii-Moriya interactions. The magnetic hysteresis loop shows  
289 low remanent magnetization ( $M_r = 1.0$  emu/g) and high coercivity ( $H_c = 23$  kOe), indicating  
290 strong magnetic anisotropy. The plate-like morphology of the crystallites with an average size  
291 of 40 nm contributes to the magnetic hardness of the sample. These results confirm the presence  
292 of magnetic ordering at RT, consistent with previously reported data for nanocrystalline  
293  $\text{YFeO}_3$ .

294 The magnetization curves  $M(H)$  of the nanocomposite, in comparison with orthoferrite  
295 samples, are shown in Fig. 5b. The  $M(H)$  curves of the BYFO samples exhibit general  
296 similarity and include hysteresis loops, indicating a consistent type of magnetic ordering at RT.  
297 Furthermore, the  $M(H)$  curves of the nanocomposites approach saturation at approximately 5  
298 kOe, which qualitatively distinguishes them from the  $\text{BiFeO}_3$  and  $\text{YFeO}_3$  curves.

299 It can also be seen that the BYFO-04-09 samples exhibit a significantly higher total  
300 magnetization  $M$  compared to the pure orthoferrite samples. Among them, the BYFO-05, -06,  
301 and -07 samples show the highest magnetic response. These samples with enhanced  
302 magnetization contain an excess of iron (see Table S2) and impurities of iron-containing  
303 magnetic phases (Fig. 1). Analysis of Mössbauer spectra revealed that the BYFO-05-06-07  
304 samples have a higher proportion of sextets corresponding to the  $\text{Fe}^{3+}$  states in magnetite  $\text{Fe}_3\text{O}_4$ ,  
305 which likely enhances the net magnetic response of these composites. In this regard,  
306 ferrimagnetism is the most probable type of ordering contributing to the enhanced magnetic  
307 response of these materials. It should be noted that the shape of the curves for all doped samples  
308 is similar to the  $M(H)$  curve of  $\text{BiFeO}_3$ , but with a significantly higher  $M$  values (the  $M(H)$   
309 curves show a characteristic loop curvature in low fields). This suggests a similar magnetic  
310 behavior of the primary phase, while the overall response is dominated by the secondary  
311 magnetic inclusions.

312 In typical  $\text{Bi}_{1-x}\text{Y}_x\text{FeO}_3$  solid solutions, the magnetization usually does not exceed 1–2  
313 emu/g, as it originates solely from canted antiferromagnetism. However, the observed  $M_s \sim 8$   
314 emu/g are characteristic of ferrimagnetic inclusions, such as  $\text{Fe}_3\text{O}_4$  clusters. Since  $M_s$  correlates  
315 with the iron excess rather than with the yttrium molar fraction ( $x$ ), these materials can be  
316 considered as nanocomposites consisting of the original bismuth and yttrium orthoferrites and  
317 magnetic iron oxides.

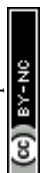


318 The physical mechanism underlying this effect in nanocomposites based on bismuth  
319 orthoferrite is the partial exchange coupling of magnetic states between  $\text{BiFeO}_3$  to other  
320 magnetic components of the nanocomposite through their interfaces [27,28]. A model  
321 describing the interaction between the magnetic moments of  $\text{Bi}_2\text{Fe}_4\text{O}_9$  and the local  
322 uncompensated moments of the antiferromagnetic  $\text{BiFeO}_3$ , mediated by a spin glass interface,  
323 was proposed in [27]. Since the BYFO nanocomposites exhibit a more complex phase  
324 composition, the exact nature of their magnetization requires further elucidation.

325 The hysteresis loop parameters for the BYFO samples are shown in Fig. 6. At room  
326 temperature, remarkably high values of saturation magnetization ( $M_{sat}$ ) and remanent  
327 magnetization ( $M_r$ ) were recorded for the BYFO-05-07 samples. This can be attributed to the  
328 iron excess  $\delta$  and the increased concentration of magnetic phases in these samples (Fig. 1). The  
329  $M_{sat}(\delta)$  curve is shown on the inset to Fig. 5.

330 Given that the Y ion is diamagnetic and possesses no intrinsic magnetic moment, the  
331  $\mu_B/\text{Y}$  value represents the degree of local decompensation within the iron antiferromagnetic  
332 sublattice induced by the dopant.  $M_{sat}$  is strongly dependent on  $\delta$  rather than the yttrium  
333 concentration alone. To gain deeper insight into the origin of magnetism in BYFO system, the  
334 effective magnetic moment per yttrium dopant ion ( $\mu_B/\text{Y}$ ) was calculated (see Table 2). The  
335 calculation of  $\mu_B/\text{Y}$  showed no systematic trend, confirming that the  $\text{Bi}^{3+} \rightarrow \text{Y}^{3+}$  substitution  
336 plays a secondary role in the macroscopic magnetic response compared to parameter  $\delta$ . The  
337 peak observed at  $x=5$  (8.1 emu/g) coincides with the maximum iron excess in this sample,  
338 suggesting the formation of uncompensated iron spin clusters that overshadow the intrinsic  
339 weak ferromagnetism of the parent phase. The  $H_c$  value also increases with increasing iron  
340 content in the samples. At  $x > 0.5$  and  $\delta > 0.5$ , the  $H_c$  value ceases to depend on the composition  
341 of the samples.

342



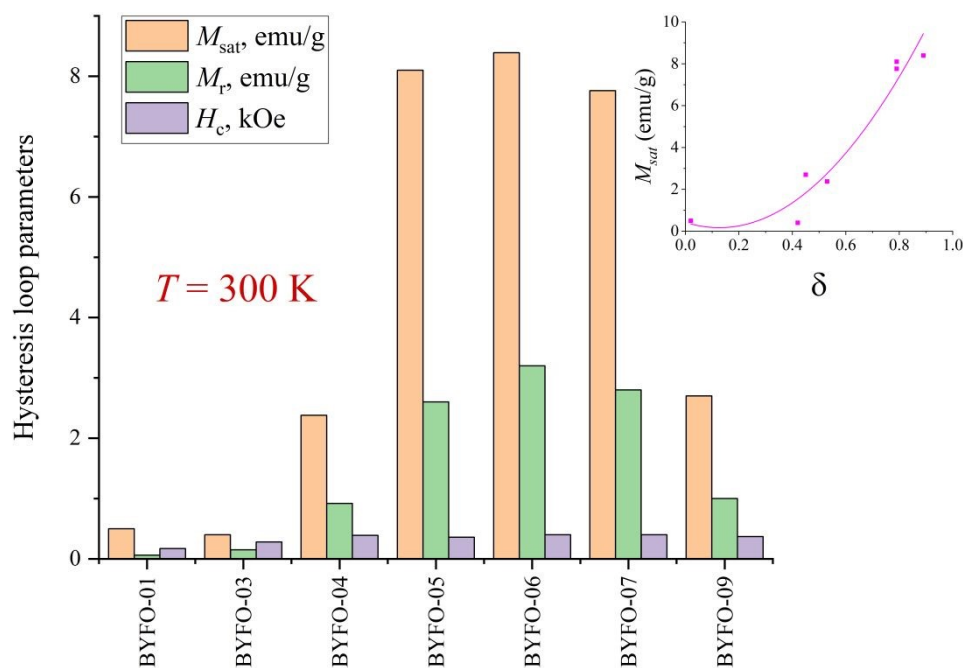


**Fig. 5.** Remnant magnetization  $M_r$ , saturation magnetization  $M_{sat}$  and coercivity  $H_c$  of the BYFO samples. Inset:  $M_{sat}$  measured at 4 kOe as a function of  $\delta$

The presence of secondary magnetic phases significantly affects the  $M_{sat}$  value, which reaches its maximum in the BYFO-05 and BYFO-06 samples. For these samples, the maximum magnetization was found to be approximately 8 emu/g at RT. As the  $\delta$  value increases,  $M_{sat}$  sharply increases (see insert to Fig. 6). This behavior of  $M_{sat}$  value correlates well with the XRD and Mössbauer data discussed above. By tuning the initial composition, we can control the parameter  $\delta$  and magnetic response of the samples. This provides a pathway to developing new materials with enhanced magnetization, which are potentially useful for nonlinear magnetic media.



343  
344  
345  
346  
347  
348  
349  
350  
351  
352  
353  
354

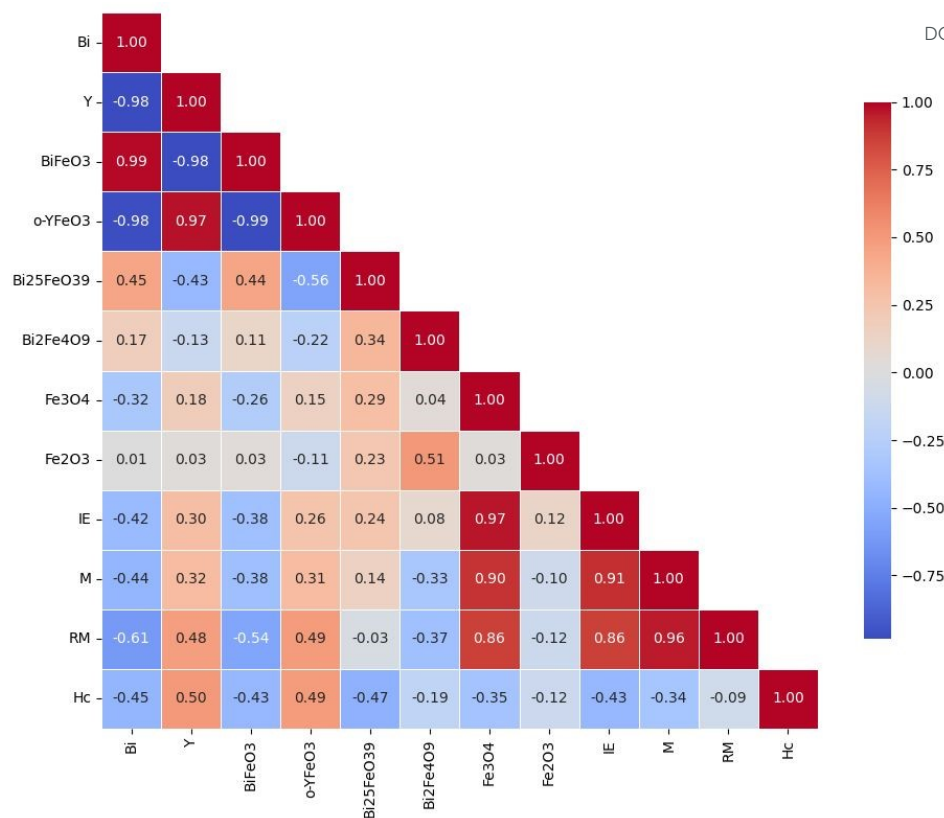
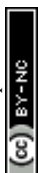


Fig. 6. Pearson's correlation matrix for magnetic properties

To establish the relationships between the composition, phase structure, and magnetic properties of BiFeO<sub>3</sub>–YFeO<sub>3</sub> nanocomposites, a correlation and regression analysis was performed using experimental data and modeling results (Fig. S3). According to the Pearson pair correlation coefficients (PCC), the bismuth content demonstrates a strong positive correlation with the BiFeO<sub>3</sub> phase (PCC = 0.99) and a strong negative correlation with *o*-YFeO<sub>3</sub> (PCC = –0.98). At the same time, for all measured magnetic parameters - iron excess (Fe<sub>excess</sub>), magnetization (M), remanent magnetization (M<sub>r</sub>), and coercivity (Hc) - the bismuth content correlates negatively (PCC from –0.42 to –0.61). In contrast, the yttrium content has a negative correlation with BiFeO<sub>3</sub> (PCC = –0.98) and a positive correlation with *o*-YFeO<sub>3</sub> (PCC = 0.97), and also correlates positively with all magnetic properties (PCC from 0.30 to 0.50). This indicates that an increase in the YFeO<sub>3</sub> content promotes an increase in magnetization and remanent magnetization, which is consistent with experimental observations: maximum values of M ≈ 8 emu/g at 4 kOe and M<sub>r</sub> ≈ 3 emu/g were recorded at x = 0.5–0.7.

Iron-containing secondary phases, which form in composites of intermediate composition, have the greatest influence on the magnetic properties. The strongest correlations are observed for magnetite Fe<sub>3</sub>O<sub>4</sub>, which is positively correlated with Fe<sub>excess</sub> (PCC = 0.97), M



355

356

357

358

359

360

361

362

363

364

365

366

367

368

369

370

371

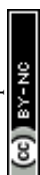
372

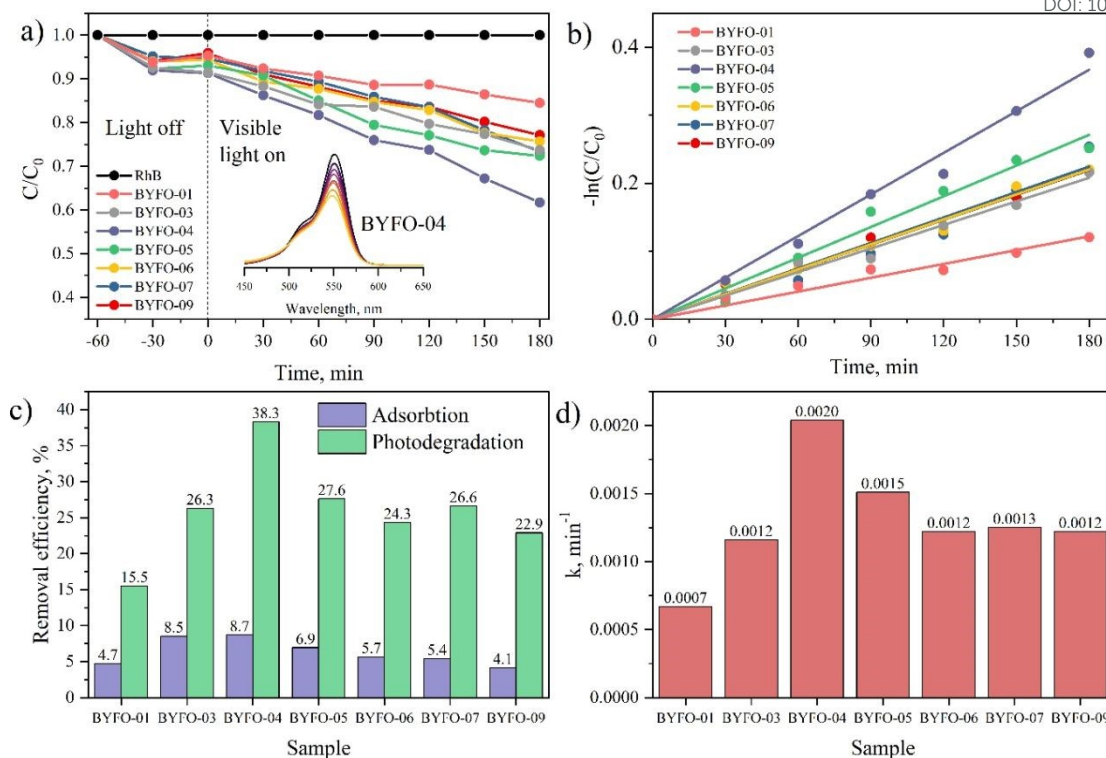
373

374 (0.90), and Mr (0.86), and only weakly negatively with Hc (−0.35). This confirms that the  
375 presence of the ferrimagnetic Fe<sub>3</sub>O<sub>4</sub> phase is the main factor enhancing the magnetic response  
376 and increasing the total magnetization in the BYFO-05–07 composites. In addition, the *o*-  
377 YFeO<sub>3</sub> phase shows positive correlations with Mr (0.49) and Hc (0.49), reflecting the  
378 contribution of crystalline anisotropy and spin canting to the increase in coercivity. In contrast,  
379 BiFeO<sub>3</sub> exhibits a negative correlation with Mr (−0.54), and the Bi<sub>25</sub>FeO<sub>39</sub> phase with Hc (−  
380 0.47), indicating their paramagnetic or weakly ferromagnetic nature, which reduces the overall  
381 magnetic response of the composite. Eight models, including polynomial regression and  
382 machine learning methods, were used to quantitatively evaluate the relationships between  
383 composition and magnetic properties (Fig. S3). The CatBoost and GPR models demonstrated  
384 the highest accuracy values ( $R^2 = 1.0$ ) for all parameters, indicating a high adequacy of the  
385 nonlinear description of the dependencies. The polynomial model also provided good results  
386 for Fe excess ( $R^2 = 0.93$ ), Mr (0.91), and M (0.84), confirming the presence of quadratic  
387 components in the composition-dependent properties. The eXGBoost and SVR models showed  
388 satisfactory results ( $R^2 = 0.50$ – $0.95$ ), while the linear ElasticNet and eLasso models did not  
389 capture the relationship ( $R^2 \approx 0$ ), indicating the complex nonlinear nature of the magnetic  
390 behavior of the composite. A combined analysis of correlations and modeling shows that  
391 enhanced magnetic properties are observed with increasing yttrium content and the formation  
392 of Fe<sub>3</sub>O<sub>4</sub> and *o*-YFeO<sub>3</sub> phases, while the predominance of BiFeO<sub>3</sub> and Bi<sub>25</sub>FeO<sub>39</sub> leads to  
393 weakening of magnetization and coercivity. The most pronounced magnetic characteristics are  
394 achieved at a BiFeO<sub>3</sub>:YFeO<sub>3</sub> ratio of  $\approx 1:1$  ( $x \approx 0.5$ – $0.7$ ), when ferrimagnetic components  
395 Fe<sub>3</sub>O<sub>4</sub> and Fe<sub>2</sub>O<sub>3</sub> form at the phase boundary, facilitating exchange interactions between the  
396 spin subsystems. This combination of antiferromagnetic and ferrimagnetic phases ensures the  
397 formation of interface-induced ferrimagnetism and explains the nonlinear increase in M and  
398 Mr with increasing YFeO<sub>3</sub> content.

### 400 3.5. Visible-light absorbance and photocatalytic activity

401 The photocatalytic properties of yttrium-doped bismuth orthoferrites were evaluated by  
402 photodegradation of the organic dye RhB in the presence of hydrogen peroxide under visible  
403 light. The temporal change in the absorption spectra during the photodegradation of the RhB  
404 solution under the influence of the BYFO-04 photocatalyst and H<sub>2</sub>O<sub>2</sub> under visible light is  
405 shown in Figure 7a. A slight shift in the main absorption peak was also observed with other  
406 samples, indicating the conversion of RhB to Rh-110 during N-deethylation indirect  
407 photodegradation in the presence of BYFO [55].





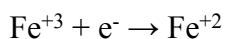
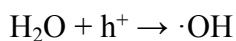
408  
409 **Fig. 7.** Photocatalytic performance of BFO-YFO samples under visible light: (a) Fenton-like  
410 degradation of dye; absorption spectra of RhB decolorization (Insert a); (b) pseudo-first-order  
411 kinetic plots; (c) Removal efficiency during adsorption and photodegradation of RhB; (d)  
412 reaction rate constants

413  
414 Figure 7c shows the time dependence of RhB photodegradation in the presence of  
415 BYFO photocatalysts and  $\text{H}_2\text{O}_2$ . When adsorption-desorption equilibrium is reached, the  
416 highest degree of adsorption is observed in the BYFO-04 sample, which is the best  
417 photocatalyst in the BYFO series. This sample photodegraded about 40% of RhB dye within  
418 180 minutes of irradiation with visible light. According to XRD data, the ratio of the main  
419 phases  $\text{BiFeO}_3/\text{YFeO}_3$  in this sample is approximately 1:1 (Fig. 2). It can be assumed that such  
420 a phase ratio ensures the creation of a stable interface between the components of the BYFO  
421 nanocomposite, which leads to an increase in its photocatalytic efficiency. A further increase  
422 in concentrations leads to a decrease in photocatalytic activity and the formation of a plateau  
423 in degradation efficiency (Fig. 7b).

424 One of the possible reasons for the highest photoactivity of the BYFO-04 sample with  
425 the addition of hydrogen peroxide to the reaction may be the presence of a photocatalytically  
426 active semiconductor  $\text{Fe}_2\text{O}_3$  in this sample (see Figure 2). Compared to other samples, the  
427 formation of the impurity compound  $\text{Fe}_2\text{O}_3$  can serve to suppress electron-hole recombination



428 by the effect of capturing electrons from the conduction band by  $\text{Fe}^{3+}$  ions and further  
 429 accelerate the Fenton-like reaction by initiating the activation of  $\text{H}_2\text{O}_2$  with the formation of  
 430 active  $\cdot\text{OH}$  radicals [34], which can be explained by the redox reaction of  $\text{Fe}^{2+}/\text{Fe}^{3+}$  ions  
 431 illustrated by the equations:

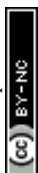


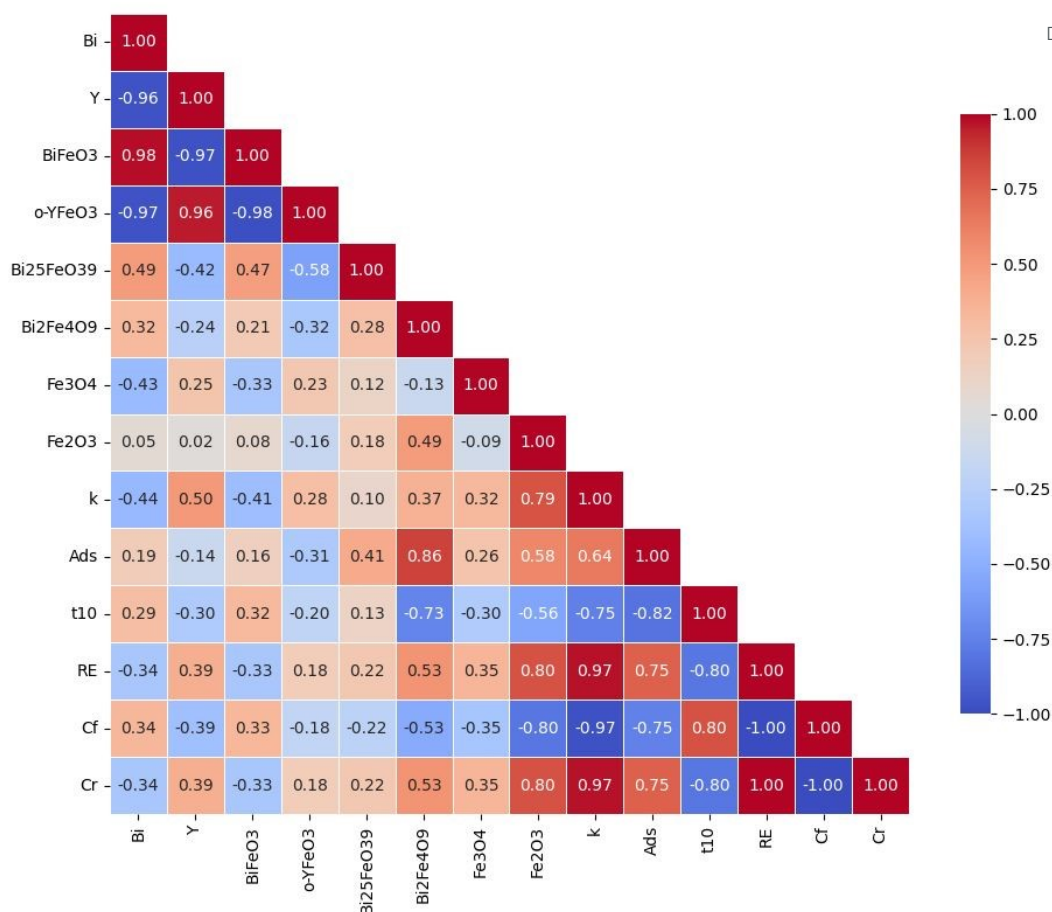
435 In Figure 10d, it can be seen that a fairly good linear correlation was found ( $R > 0.98$ ),  
 436 indicating that the reaction is a pseudo-first order reaction. To quantitatively understand the  
 437 kinetics of the RhB degradation reaction, a pseudo-first order model expressed by Equation  
 438 (2), which is typically used at low initial contaminant concentrations, was applied [56]. As  
 439 stated above, the presence of impurity iron oxides in BYFO-04 leads to an increase in the  
 440 photodegradation rate constant to  $k=2.04 \cdot 10^{-3} \text{ min}^{-1}$ .

$$441 \quad \ln\left(\frac{C_0}{C}\right) = kt \quad (2)$$

442 where  $C_0$  is the initial concentration of the dye,  $C$  is the concentration of the dye after  $t$   
 443 minutes,  $k$  is the reaction rate constant ( $\text{min}^{-1}$ ),  $t$  is time.

444 To determine the compositional dependence of the photocatalytic activity of  $\text{BiFeO}_3$ -  
 445  $\text{YFeO}_3$  nanocomposites, a correlation and regression analysis was performed using  
 446 experimental parameters ( $k$ , RE,  $C_{\text{reacted}}$ ,  $C_{\text{final}}$ ,  $t_{10\%}$ , Ads) (Fig. 8). According to the calculations  
 447 of the Pearson pair correlation coefficients (PCC), the bismuth content has a strong positive  
 448 correlation with the  $\text{BiFeO}_3$  phase (PCC = 0.98) and a strong negative correlation with the  $o$ -  
 449  $\text{YFeO}_3$  phase (PCC = -0.97). For photocatalytic parameters, a negative correlation is observed  
 450 between the bismuth content and the rate constant ( $k$ , -0.44), the decomposition efficiency (RE,  
 451 -0.34), and the amount of reacted substance ( $C_{\text{reacted}}$ , -0.34), while a positive correlation is  
 452 observed with the final dye concentration ( $C_{\text{final}}$ , 0.34), the time to reach 10% degradation ( $t_{10\%}$ ,  
 453 0.29), and the degree of adsorption (Ads, 0.19). Thus, an increase in the  $\text{BiFeO}_3$  proportion is  
 454 accompanied by a decrease in photocatalytic activity. In contrast, increasing the yttrium  
 455 content, which correlates negatively with  $\text{BiFeO}_3$  (PCC = -0.97) and positively with  $o$ - $\text{YFeO}_3$   
 456 (PCC = 0.96), has the opposite effect: for the  $k$ , RE, and  $C_{\text{reacted}}$  parameters, the correlation  
 457 is positive (0.39–0.50), while for Ads,  $t_{10\%}$ , and  $C_{\text{final}}$ , it is negative (-0.14 to -0.39). This  
 458 indicates that increasing the proportion of  $\text{YFeO}_3$  and associated oxide phases accelerates  
 459 photodegradation and increases the efficiency of organic compound decomposition under the  
 460 influence of visible light.





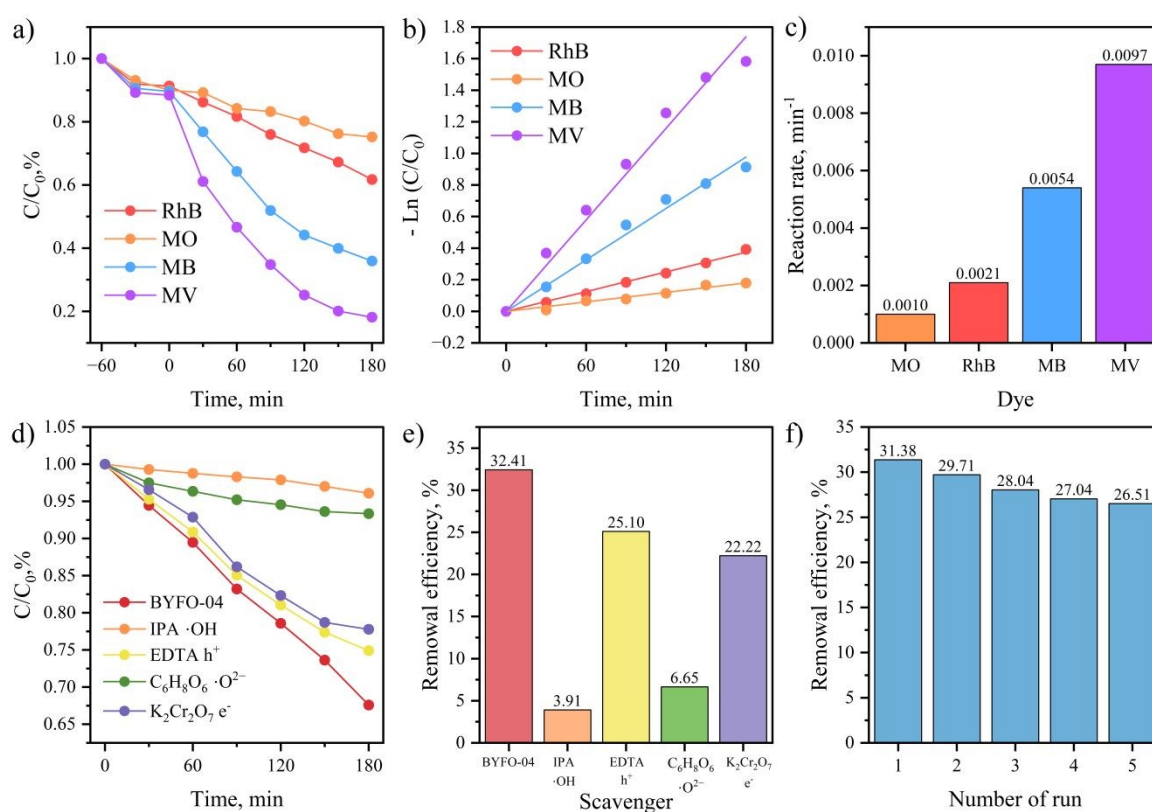
461  
462 **Fig. 8** Pearson's correlation matrix for photocatalytic properties

463  
464 The contribution of secondary phases should be noted separately. The appearance of  
465 the  $\text{Bi}_2\text{Fe}_4\text{O}_9$  phase is accompanied by a strong positive correlation with Ads (0.86), RE (0.53),  
466  $C_{\text{reacted}}$  (0.53) and a negative one with  $t_{10\%}$  (-0.73),  $C_{\text{final}}$  (-0.53), indicating an increase in  
467 photo-Fenton-like activity with increasing its content. Similarly, the  $\text{Fe}_2\text{O}_3$  phase exhibits a  
468 positive correlation with Ads (0.58), RE (0.80),  $C_{\text{reacted}}$  (0.80) and a negative one with  $t_{10\%}$  (-  
469 0.56),  $C_{\text{final}}$  (-0.80), confirming its role in accelerating dye degradation processes due to the  
470 generation of active  $\cdot\text{OH}$  radicals.

471 Eight models, including polynomial regression and machine learning algorithms, were  
472 used to quantitatively describe the dependencies (Fig. S4). The best results across all  
473 parameters were achieved for the CatBoost ( $R^2 = 1.0$ ) and GPR ( $R^2 = 0.94\text{--}1.0$ ) models,  
474 confirming the presence of pronounced nonlinear relationships between composition and  
475 photocatalytic performance. The polynomial model demonstrated high  $R^2$  values for Ads  
476 (0.996), k (0.93),  $t_{10\%}$  (0.96), and RE (0.89), indicating an adequate description of the effect  
477 through a quadratic relationship. The eXGBoost and SVR algorithms showed moderate results  
478 ( $R^2 = 0.45\text{--}0.76$ ), while the ElasticNet and eLasso linear models were unable to capture the



479 patterns ( $R^2 \approx 0$ ), confirming the complex nonlinear nature of photodegradation processes in  
 480 heterogeneous systems. Thus, the simulation confirmed that increasing the yttrium content and  
 481 the formation of the  $\text{YFeO}_3$  phase, as well as the presence of photocatalytically active  $\text{Fe}_2\text{O}_3$   
 482 and  $\text{Bi}_2\text{Fe}_4\text{O}_9$  phases, contribute to an increase in the degradation rate of organic dyes and an  
 483 increase in the efficiency of photocatalysis. The highest values of the rate constant ( $k = 2.04$   
 484  $10^{-3} \text{ min}^{-1}$ ) and degradation efficiency (RE) are observed in samples with a close ratio of  
 485  $\text{BiFeO}_3:\text{YFeO}_3 \approx 1:1$  ( $x \approx 0.4-0.5$ ), which is consistent with the experimental results and  
 486 confirms the role of interfacial interactions in enhancing photo-Fenton-like processes.  
 487



488 **Fig. 9** Photocatalytic performance of BYFO-04 sample under visible light: (a) Fenton-like  
 489 degradation of dyes; (b) pseudo-first-order kinetic plots; (c) reaction rate constants; (d-e)  
 490 scavenger tests for RhG photodegradation; (f) cyclic stability test.

491

492 To assess the practical applicability of the synthesized BYFO-04 photocatalyst, its  
 493 photocatalytic activity was evaluated using a range of model organic dyes (Fig. 9 a-c). The  
 494 material demonstrated high degradation efficiency toward thiazine and triarylmethane dyes,  
 495 achieving 65% and 80% decomposition of methylene blue and methyl violet, respectively. In  
 496 contrast, the degradation efficiency for azo dyes was limited to approximately 25%, which can



497 be attributed to their greater structural stability under the applied conditions. Reaction rate  
498 constants are presented in Fig. 9 d.

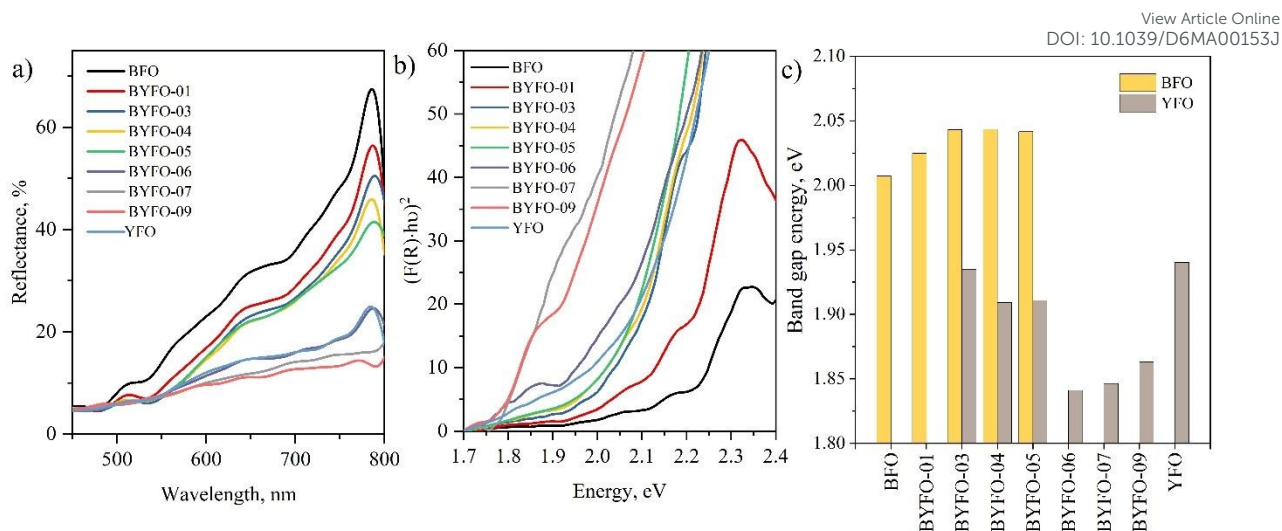
499 To elucidate the mechanism of the Fenton-like degradation of rhodamine B catalyzed  
500 by the synthesized material, a series of radical scavenging experiments were conducted (Fig. 9  
501 d-e). Ascorbic acid was employed to scavenge superoxide radicals ( $\cdot\text{O}_2^-$ ), isopropyl alcohol  
502 (IPA) was used to trap hydroxyl radicals ( $\cdot\text{OH}$ ), disodium ethylenediaminetetraacetate (EDTA)  
503 served as a hole ( $\text{h}^+$ ) scavenger, and potassium dichromate ( $\text{K}_2\text{Cr}_2\text{O}_7$ ) was utilized to capture  
504 photogenerated electrons ( $\text{e}^-$ ). The results indicate that hydroxyl radicals ( $\cdot\text{OH}$ ) and superoxide  
505 radicals ( $\cdot\text{O}_2^-$ ) play dominant roles in the degradation process, whereas photogenerated holes  
506 ( $\text{h}^+$ ) and electrons ( $\text{e}^-$ ) contribute to a lesser extent [57]. Moreover, cyclic stability tests revealed  
507 a gradual decline in catalytic activity, with an approximate 5% loss in efficiency observed by  
508 the fifth cycle (Fig. 9 f).

509 The diffuse reflectance spectra of the samples presented in Fig. 10a. All the samples  
510 demonstrate low reflectance at 400-550 nm that indicates the effective absorbance of visible  
511 light spectrum. The bends of curves demonstrate the strong interaction with visible light in its  
512 full diapason for all samples. It can be noticed that the reflection rate systematically decreases  
513 with increase of yttrium content, except YFO sample. The band gap energy values were  
514 evaluated by extrapolation of the linear Tauc plots parts (Fig. 10b) and summarized in Table  
515 S4. The band gap energy values (Fig. 9c) for the BFO and YFO samples were 2.0 and 1.94 eV,  
516 respectively, which is close to previous reports (4, 14). The  $E_g$  values of  $\text{BiFeO}_3$  slightly  
517 increase with increase of yttrium content up to 2.04 eV, within the error of the determination  
518 method. For the *o*- $\text{YFeO}_3$  phase (BYFO-0.3-0.5, 1) there is the same behavior with insignificant  
519 change of band gap energy. However, for the several samples (BYFO-0.6-0.9) the noticeable  
520 decrease of  $E_g$  is observed, which can be associated with their solid-solution nature.

521 The band gap structure parameters were evaluated by followed empirical formulas:  $E_{VB}$   
522  $= \chi - E_e + 0.5 \cdot E_g$  and  $E_{CB} = E_{VB} - E_g$ , where  $E_e = 4.5$ ;  $\chi$  is electronegativity  $\chi$  (YFO) = 5.60 eV,  
523  $\chi$  (BFO) = 5.89 eV. The calculated values of the conduction band edge potential ( $E_{CB}$ ) and  
524 valence band edge potentials ( $E_{VB}$ ) are presented in Table S4 and the band gap structure of the  
525 Y04 is visualized in Fig.10.

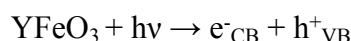
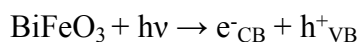
526



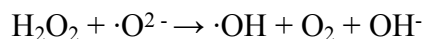
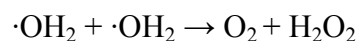
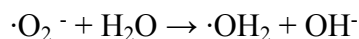
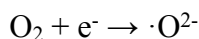
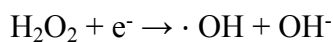
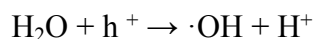
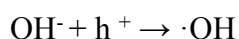


527  
528 **Fig. 10.** Diffuse reflectance spectra (a), Tauc plots (b), and band gap energy values (c) of the  
529 BFO-YFO samples.

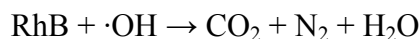
530  
531 The activity of both nanocomposite materials under visible light irradiation ( $E_g$  (BFO)  
532 = 2.04 eV,  $E_g$  (YFO) = 1.91 eV) was previously mentioned.



535 The calculated CB and VB values were 0.37 eV and 2.41 eV for BFO, and 0.16 eV and  
536 2.05 eV for YFO providing the heterojunction formation. The possibility electron transfer from  
537 YFeO<sub>3</sub> CB to BiFeO<sub>3</sub> CB and hole transfer from BiFeO<sub>3</sub> VB to YFeO<sub>3</sub> VB prevents the coupling  
538 of electron-hole pairs and increases photocatalytic activity (Figure 11). The wide band gaps  
539 and high VB values of both nanocomposite components make feasible several ·OH radical  
540 generation reactions.



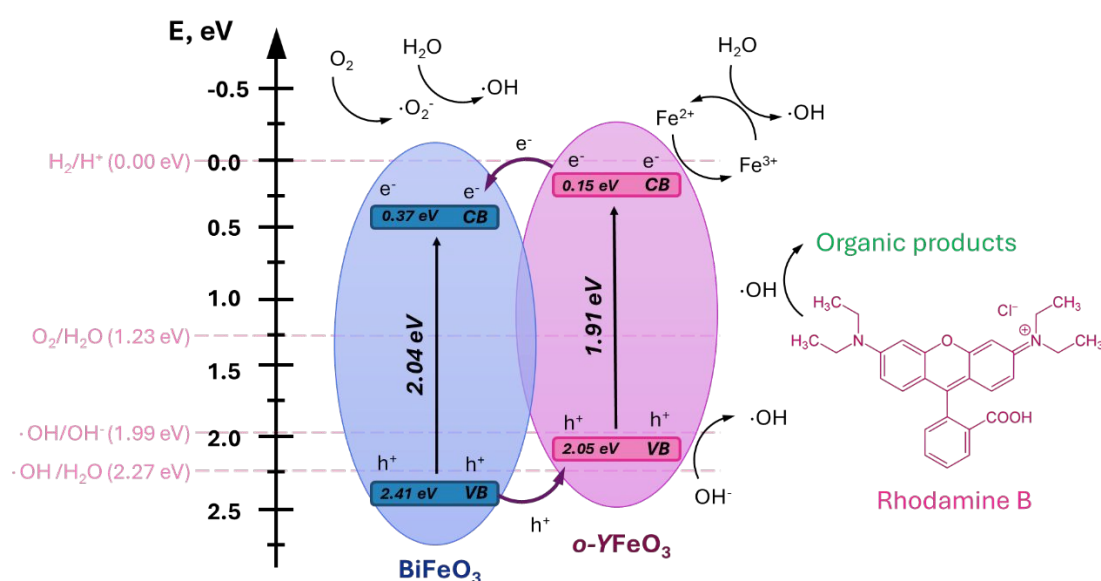
548 The ·OH radicals are known to be very effective in organic pollutants degradation.



550 The presence of  $\text{Fe}^{3+}$  ions in both nanocomposite materials leads to multiple  $\cdot\text{OH}$  radicals' generation in Fenton-like process.



552 That explains the high photocatalytic activity of the  $\text{BiFeO}_3\text{-YFeO}_3$  heterojunction nanocomposite in the process of Fenton-like photodegradation of RhB. The reduced electron-hole pairs coupling increased  $\cdot\text{OH}$  radicals' generation, and high level of visible light absorption make this photocatalyst a promising material for advanced oxidation processes of organic pollutants decomposition.

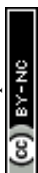


560 **Fig. 11.** Mechanism of photo-Fenton degradation of RhB over BFO-YFO nanocomposites

561 An increase in the photocatalytic activity of  $\text{BiFeO}_3\text{-YFeO}_3$  nanocomposites can be  
 562 realized by varying the iron content in the target product, which can be influenced by synthesis  
 563 conditions, such as the type of organic fuel and the fuel/oxidizer ratio in the initial composition.  
 564 Properties such as magnetically ordered state at room temperature and obvious photocatalytic  
 565 activity of the synthesized materials are promising for efficient separation of the photocatalyst  
 566 from the reaction medium.

#### 570 4. Conclusion

571 Nanocrystalline materials based on the  $x\text{BiFeO}_3\text{-(1-x)YFeO}_3$  system were synthesized  
 572 using the glycine-nitrate combustion method. The obtained materials have an average  
 573 crystallite size in the range of 25–90 nm. XRD and EDX data demonstrated the effect of the



574 initial composition on the phase composition of the target product. At nominal values of  $x =$   
575 0.3-0.7, nanocomposites samples were formed. It was found that BYFO-04 nanocomposite  
576 with a ratio approximately 1:1 between bismuth and yttrium orthoferrites, exhibits increased  
577 photocatalytic activity compared to the other samples.

578 The magnetic properties of the obtained materials were investigated by Mössbauer  
579 spectroscopy and magnetometry. At RT, all synthesized materials exhibit magnetic order. The  
580 results showed that the BYFO materials have improved magnetic properties, demonstrating in  
581 an increase in total magnetization by several times compared to pure orthoferrites. The BYFO-  
582 0.5 and BYFO-0.7 nanocomposites showed an improved magnetic response, with specific and  
583 saturation magnetization values of approximately 8 emu/g at a field of 4 kOe. The discovered  
584 properties of the synthesized materials are promising for the effective separation of  
585 photocatalysts from the reaction medium.

#### 586 **Author contributions**

587 **S. M. Tikhanova** – Formal analysis, Investigation, Visualization, Writing – original draft,  
588 Writing – review & editing; **M.P. Volkov** – Data curation, Formal analysis, Investigation; **I.V.**  
589 **Buryanenko** – Data curation, Formal analysis, Investigation; **V.G. Semenov** – Data curation,  
590 Formal analysis, Investigation; **Zh. Orazovd** –Data curation, Formal analysis, Investigation;  
591 **V.I. Romanovski** - Data curation, Formal analysis, Investigation, Visualization, Writing –  
592 original draft, Writing – review & editing; **V.I. Popkov** – Project administration, Supervision,  
593 Validation, Writing – review & editing; **N.A. Lomanova** - Conceptualization, Methodology,  
594 Project administration, Supervision, Validation, Writing – review & editing.

#### 595 **Acknowledgments**

596 The authors are grateful to Victor V. Gusarov (Ioffe Institute, St. Petersburg, Russia) for fruitful  
597 discussions and advices.

#### 600 **Conflict of interest**

601 The authors declare no competing interests.

#### 602 **Data Availability Statement**

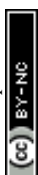
603 The data that support the findings of this study are available from the corresponding author  
604 upon reasonable request.

605

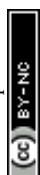


608 **References**

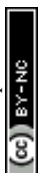
- 609 [1] J.F. Scott, Data storage: Multiferroic memories, *Nat. Mater.* 6 (2007) 256–257.  
610 <https://doi.org/10.1038/NMAT1868>;KWRD.
- 611 [2] A.R. Akbashev, A.R. Kaul, A.R. Akbashev, A.R. Kaul, Structural and chemical aspects  
612 of the design of multiferroic materials, *RuCRv.* 80 (2011) 1159–1177.  
613 <https://doi.org/10.1070/RC2011V080N12ABEH004239>.
- 614 [3] Y. Chen, J. Yang, X. Wang, F. Feng, Y. Zhang, Y. Tang, Synthesis YFeO<sub>3</sub> by salt-  
615 assisted solution combustion method and its photocatalytic activity, *J. Ceram. Soc. Japan.* 122  
616 (2014) 146–150. <https://doi.org/10.2109/JCERSJ2.122.146>.
- 617 [4] N. Wang, X. Luo, L. Han, Z. Zhang, R. Zhang, H. Olin, Y. Yang, Structure,  
618 Performance, and Application of BiFeO<sub>3</sub> Nanomaterials, *Nano-Micro Lett.* 12 (2020) 1–23.  
619 <https://doi.org/10.1007/S40820-020-00420-6>/FIGURES/3.
- 620 [5] O. Rosales-González, F. Sánchez-De Jesús, M.A. Camacho-González, C.A. Cortés-  
621 Escobedo, A.M. Bolarín-Miró, Synthesis of magnetically removable photocatalyst based on  
622 bismuth doped YFeO<sub>3</sub>, *Mater. Sci. Eng. B.* 261 (2020) 114773.  
623 <https://doi.org/10.1016/j.mseb.2020.114773>.
- 624 [6] V. Venugopal, D. Balaji, M. Preeyanghaa, C.J. Moon, B. Neppolian, G. Muthusamy, J.  
625 Theerthagiri, J. Madhavan, M.Y. Choi, Synergistic combination of BiFeO<sub>3</sub> nanorods and  
626 CeVO<sub>4</sub> nanoparticles for enhanced visible light driven photocatalytic activity, *Alexandria Eng.*  
627 *J.* 72 (2023) 531–543. <https://doi.org/10.1016/J.AEJ.2023.04.024>.
- 628 [7] L.A. Al-Hajji, H. Alshaikh, M.H.H. Mahmoud, A.A. Ismail, Soft Template-Assisted  
629 Controllable Synthesis of Nanocrystalline Orthorhombic YFeO<sub>3</sub> Decorated Porous g-C<sub>3</sub>N<sub>4</sub>  
630 with Enhanced Hg(II) reduction, *J. Inorg. Organomet. Polym. Mater.* 31 (2021) 4150–4162.  
631 <https://doi.org/10.1007/S10904-021-02022-0>/FIGURES/8.
- 632 [8] G.M. Alsulaim, K.M. Alnahdi, New magnetic nanoscaled AlVCe-Cr<sub>2</sub>O<sub>3</sub>  
633 semiconductors for opto- and spin-transport electronics, *Alexandria Eng. J.* 132 (2025) 169–  
634 180. <https://doi.org/10.1016/j.aej.2025.10.029>.
- 635 [9] J. Wu, Z. Fan, D. Xiao, J. Zhu, J. Wang, Multiferroic bismuth ferrite-based materials  
636 for multifunctional applications: Ceramic bulks, thin films and nanostructures, *Prog. Mater.*  
637 *Sci.* 84 (2016) 335–402. <https://doi.org/10.1016/J.PMATSCI.2016.09.001>.
- 638 [10] X. Li, Z. Tang, H. Ma, F. Wu, R. Jian, PVP-assisted hydrothermal synthesis and  
639 photocatalytic activity of single-crystalline BiFeO<sub>3</sub> nanorods, *Appl. Phys. A Mater. Sci.*  
640 *Process.* 125 (2019) 1–6. <https://doi.org/10.1007/S00339-019-2892-2>/FIGURES/6.



- 641 [11] T.D. Trinh, N.A. Tien, V.O. Mittova, B.N.V. Phuong, T.T.T. Ngan, T.T.T. Nga, N. Van  
642 My, I.Y. Mittova, E.V. Tomina, L.T.T. Thuy, T.S. Cam, Studying the influence of synthesis  
643 conditions on the magnetic properties of perovskite-like  $\text{YbFeO}_3$  nanomaterials, *J. Solid State*  
644 *Chem.* 328 (2023) 124377. <https://doi.org/10.1016/J.JSSC.2023.124377>.
- 645 [12] N.A. Tien, N.T. Trang, V.O. Mittova, N.T. Lan, N.T.T. Nhan, C.H. Diem, T.C. Hien,  
646 I.Y. Mittova, B.X. Vuong, Structural, thermal, and magnetic properties of orthoferrite  $\text{EuFeO}_3$   
647 nanoparticles prepared by a simple co-precipitation method, *J. Mater. Sci. Mater. Electron.* 34  
648 (2023) 1–10. <https://doi.org/10.1007/S10854-023-10779-Y/TABLES/2>.
- 649 [13] A.S. Seroglazova, M.I. Chebanenko, V.N. Nevedomskiy, V.I. Popkov, Solution  
650 combustion synthesis of novel  $\text{PrFeO}_3/\text{CeO}_2$  nanocomposite with enhanced photo-Fenton  
651 activity under visible light, *Ceram. Int.* 49 (2023) 15468–15479.  
652 <https://doi.org/10.1016/J.CERAMINT.2023.01.132>.
- 653 [14] T.S. Cam, A.S. Seroglazova, M.I. Chebanenko, B. Mardiyev, E.V. Dzhevaga, O.V.  
654 Almjasheva, V.I. Popkov, Colloidal solution combustion synthesis of am- $\text{TiO}_2/\text{o-YFeO}_3$   
655 nanocomposites: effect of titania loading on the photo-Fenton-like activity, *J. Sol-Gel Sci.*  
656 *Technol.* 108 (2023) 502–513. <https://doi.org/10.1007/S10971-023-06206-7/FIGURES/11>.
- 657 [15] S. Tikhanova, A. Seroglazova, M. Chebanenko, V. Nevedomskiy, V. Popkov, Effect of  
658  $\text{TiO}_2$  Additives on the Stabilization of h- $\text{YbFeO}_3$  and Promotion of Photo-Fenton Activity of  
659 o- $\text{YbFeO}_3/\text{h-YbFeO}_3/\text{r-TiO}_2$  Nanocomposites, *Materials (Basel)*. 15 (2022).  
660 <https://doi.org/10.3390/ma15228273>.
- 661 [16] Y. Albadi, M.S. Ivanova, L.Y. Grunin, R.A. Makarin, A.S. Komlev, M.I. Chebanenko,  
662 V.N. Nevedomskiy, V.I. Popkov, Ultrasound-assisted co-precipitation synthesis of  $\text{GdFeO}_3$   
663 nanoparticles: structure, magnetic and MRI contrast properties, *Phys. Chem. Chem. Phys.* 24  
664 (2022) 29014–29023. <https://doi.org/10.1039/D2CP03688F>.
- 665 [17] G.M. Alsulaim, New photocatalysts stimulated by visible light for organic-waste  
666 remediation: (La/Ce) and (La/Gd) codoped  $\text{BiFeO}_3$ , *J. Mater. Sci. Mater. Electron.* 34 (2023).  
667 <https://doi.org/10.1007/s10854-023-11671-5>.
- 668 [18] G.M. Alsulaim, Ferromagnetic nature and solar-induced fast catalytic properties for  
669 green environment: New Fe/Cu/V- $\text{Mn}_3\text{O}_4$  p-type compounds, *Arab. J. Chem.* 18 (2025)  
670 1342025. [https://doi.org/10.25259/ajc\\_134\\_2025](https://doi.org/10.25259/ajc_134_2025).
- 671 [19] D.C. Arnold, K.S. Knight, F.D. Morrison, P. Lightfoot, Ferroelectric-paraelectric  
672 transition in  $\text{BiFeO}_3$ : Crystal structure of the orthorhombic  $\beta$  phase, *Phys. Rev. Lett.* 102  
673 (2009). <https://doi.org/10.1103/PHYSREVLETT.102.027602>.



- 674 [20] H. Shen, J. Xu, A. Wu, J. Zhao, M. Shi, Magnetic and thermal properties of perovskite  
675  $\text{YFeO}_3$  single crystals, *Mater. Sci. Eng. B.* 157 (2009) 77–80.  
676 <https://doi.org/10.1016/J.MSEB.2008.12.020>.
- 677 [21] Z. Zhou, L. Guo, H. Yang, Q. Liu, F. Ye, Hydrothermal synthesis and magnetic  
678 properties of multiferroic rare-earth orthoferrites, *J. Alloys Compd.* 583 (2014) 21–31.  
679 <https://doi.org/10.1016/J.JALLCOM.2013.08.129>.
- 680 [22] A. Haruna, I. Abdulkadir, S.O. Idris, Photocatalytic activity and doping effects of  
681  $\text{BiFeO}_3$  nanoparticles in model organic dyes, *Heliyon.* 6 (2020) e03237.  
682 <https://doi.org/10.1016/J.HELIYON.2020.E03237>.
- 683 [23] K.D. Martinson, V.A. Ivanov, M.I. Chebanenko, V. V. Panchuk, V.G. Semenov, V.I.  
684 Popkov, Facile combustion synthesis of  $\text{TbFeO}_3$  nanocrystals with hexagonal and  
685 orthorhombic structure, *Nanosyst. Physics, Chem. Math.* 10 (2019) 694–700.  
686 <https://doi.org/10.17586/2220-8054-2019-10-6-694-700>.
- 687 [24] Y. Subramanian, V. Ramasamy, R.J. Karthikeyan, G.R. Srinivasan, D. Arulmozhi, R.K.  
688 Gubendiran, M. Sriramalu, Investigations on the enhanced dye degradation activity of  
689 heterogeneous  $\text{BiFeO}_3$ – $\text{GdFeO}_3$  nanocomposite photocatalyst, *Heliyon.* 5 (2019) e01831.  
690 <https://doi.org/10.1016/J.HELIYON.2019.E01831>.
- 691 [25] N. V. Besprozvannykh, D.S. Ershov, O.Y. Sinelshchikova,  $\text{SrO}$ – $\text{BiP}_2\text{O}_3$ – $\text{Fe}_2\text{O}_3$ -Based  
692 Composites: Synthesis and Electrophysical Properties, *Russ. J. Gen. Chem.* 89 (2019) 2458–  
693 2462. <https://doi.org/10.1134/S1070363219120211/METRICS>.
- 694 [26] M.S. Lomakin, O. V. Proskurina, D.P. Danilovich, V. V. Panchuk, V.G. Semenov, V.  
695 V. Gusarov, Hydrothermal synthesis, phase formation and crystal chemistry of the  
696 pyrochlore/ $\text{Bi}_2\text{WO}_6$  and pyrochlore/ $\alpha$ - $\text{Fe}_2\text{O}_3$  composites in the  $\text{Bi}_2\text{O}_3$ – $\text{Fe}_2\text{O}_3$ – $\text{WO}_3$  system, *J.*  
697 *Solid State Chem.* 282 (2020) 121064. <https://doi.org/10.1016/J.JSSC.2019.121064>.
- 698 [27] I. V. Pleshakov, M.P. Volkov, N.A. Lomanova, Y.I. Kuz'min, V. V. Gusarov, Magnetic  
699 Characteristics of a Nanocomposite Based on Bismuth Ferrites, *Tech. Phys. Lett.* 46 (2020)  
700 1072–1075. <https://doi.org/10.1134/S1063785020110115/FIGURES/3>.
- 701 [28] T. Maity, S. Roy, Asymmetric ascending and descending loop shift exchange bias in  
702  $\text{Bi}_2\text{Fe}_4\text{O}_9$ – $\text{BiFeO}_3$  nanocomposites, *J. Magn. Magn. Mater.* 494 (2020) 165783.  
703 <https://doi.org/10.1016/J.JMMM.2019.165783>.
- 704 [29] L. Tian, P. an Gao, F. gang Wang, X. wei Li, G. Li, Study on Preparation of  
705  $\text{BiFeO}_3$ / $\text{Bi}_2\text{Fe}_4\text{O}_9$  Composite Photocatalyst and Photocatalytic Degradation of Various Organic  
706 Dyes in Waste Water, *Russ. J. Phys. Chem. A.* 95 (2021) 1495–1504.  
707 <https://doi.org/10.1134/S0036024421070177/FIGURES/13>.



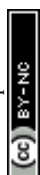
- 708 [30] S.M. Yakout, A.M. Youssef, M.A. Wahba, W. Sharmoukh, A.M. El Sayed, M.S. Khalil, Superior ferromagnetic and electrical properties: High purity multiferroic  
709  $\text{Bi}_{0.98}\text{M}_{0.02}\text{FeO}_3$  (M = La, Pr, Gd) compositions, *J. Magn. Magn. Mater.* 561 (2022) 169751.  
710 <https://doi.org/10.1016/j.jmmm.2022.169751>.
- 711 [31] M.A. Wahba, S.M. Yakout, A.M. Youssef, W. Sharmoukh, A.M.E. sayed, M.S. Khalil,  
712 Chelating Agents Assisted Rapid Synthesis of High Purity  $\text{BiFeO}_3$ : Remarkable Optical,  
713 Electrical, and Magnetic Characteristics, *J. Supercond. Nov. Magn.* 2022 3512. 35 (2022)  
714 3689–3704. <https://doi.org/10.1007/s10948-022-06425-z>.
- 715 [32] N.A. Lomanova, I. V. Pleshakov, M.P. Volkov, S.G. Yastrebov, K. Kenges, V.L.  
716 Ugolkov, A. V. Osipov, T. Siyuan, I. V. Buryanenko, V.G. Semenov, Solution combustion  
717 synthesis of  $\text{Bi}_2\text{Fe}_4\text{O}_9$  possessing enhanced magnetic and photocatalytic properties, *Inorg.*  
718 *Chem. Commun.* 161 (2024) 112109. <https://doi.org/10.1016/J.INOCHE.2024.112109>.
- 719 [33] A.A. Ostroushko, T.Y. Maksimchuk, A.E. Permyakova, O. V. Russkikh, Determinative  
720 Factors for the Thermochemical Generation of Electric Charges upon Combustion of Nitrate–  
721 Organic Precursors for Materials Based on Lanthanum Manganite and Cerium Dioxide, *Russ.*  
722 *J. Inorg. Chem.* 67 (2022) 799–809.  
723 <https://doi.org/10.1134/S0036023622060171/FIGURES/6>.
- 724 [34] Z. Shang, T. Wang, A. Ren, Y. Yu, Y. Zheng, Y. Tao, P. Feng, Y. Xiao, X. Wang,  
725 Hollow macroporous  $\text{CeO}_2/\beta\text{-Bi}_2\text{O}_3$  heterostructure sphere via one-step spray solution  
726 combustion synthesis for efficient photocatalysis, *Appl. Surf. Sci.* 619 (2023) 156718.  
727 <https://doi.org/10.1016/J.APSUSC.2023.156718>.
- 728 [35] Z. Shang, Z. Yang, Y. Xiao, X. Wang, Ordered mesoporous  $\text{Ag}/\text{CeO}_2$  nanocrystalline  
729 via silica-templated solution combustion for enhanced photocatalytic performance, *Colloids*  
730 *Surfaces A Physicochem. Eng. Asp.* 604 (2020) 125301.  
731 <https://doi.org/10.1016/J.COLSURFA.2020.125301>.
- 732 [36] Z. Shang, Y. Yu, H. Yang, Z. Yang, Y. Xiao, X. Wang, One-step solution combustion  
733 synthesis of micro-nano-scale porous  $\text{Cu}/\text{CeO}_2$  with enhanced photocatalytic properties, *J.*  
734 *Rare Earths.* 41 (2023) 250–258. <https://doi.org/10.1016/J.JRE.2022.02.013>.
- 735 [37] A.A. Ostroushko, I.D. Gagarin, E. V. Kudyukov, T.Y. Zhulanova, A.E. Permyakova,  
736 O. V. Russkikh, Synthesis of lanthanum manganite powders via combustion reactions: some  
737 aspects of the influence of magnetic field and charge generation in precursors on the formation  
738 of properties, *Nanosyst. Physics, Chem. Math.* 14 (2025) 571–583.  
739 <https://doi.org/10.17586/2220-8054-2023-14-5-571-583>.
- 740



- 741 [38] E.A. Tugova, O.N. Karpov, S.G. Yastrebov, Raman scattering features of  
742 nanocrystalline neodymium ferrite, *Nano-Structures & Nano-Objects*. 33 (2023) 100946.  
743 <https://doi.org/10.1016/J.NANOSO.2023.100946>.
- 744 [39] J.L. Ortiz-Quiñonez, D. Díaz, I. Zumeta-Dubé, H. Arriola-Santamaría, I. Betancourt, P.  
745 Santiago-Jacinto, N. Nava-Etzana, Easy synthesis of high-purity BiFeO<sub>3</sub> nanoparticles: New  
746 insights derived from the structural, optical, and magnetic characterization, *Inorg. Chem.* 52  
747 (2013) 10306–10317.  
748 [https://doi.org/10.1021/IC400627C/SUPPL\\_FILE/IC400627C\\_SI\\_002.AVI](https://doi.org/10.1021/IC400627C/SUPPL_FILE/IC400627C_SI_002.AVI).
- 749 [40] V.I. Popkov, M.I. Chebanenko, M.I. Tenevich, I. V. Buryanenko, V.G. Semenov,  
750 Solution combustion synthesis of iron-deficient Sc<sub>2-x</sub>Fe<sub>x</sub>O<sub>3</sub> (x = 0.17-0.47) nanocrystals with  
751 bixbyite structure: The effect of spatial constraints, *Ceram. Int.* 48 (2022) 36046–36055.  
752 <https://doi.org/10.1016/j.ceramint.2022.08.027>.
- 753 [41] Buryanenko I. V., Semenov V. G., Lomanova N. A., Osipov A. V., Volkov M. P.,  
754 Pleshakov I. V., Magnetic properties of nanocrystalline material based on Bi<sub>2</sub>Fe<sub>4</sub>O<sub>9</sub>, *Phys.*  
755 *Solid State.* 64 (2022) 539. <https://doi.org/10.21883/PSS.2022.05.53513.274>.
- 756 [42] V.I. Popkov, O. V. Almjasheva, V.N. Nevedomskiy, V. V. Panchuk, V.G. Semenov,  
757 V. V. Gusarov, Effect of spatial constraints on the phase evolution of YFeO<sub>3</sub>-based  
758 nanopowders under heat treatment of glycine-nitrate combustion products, *Ceram. Int.* 44  
759 (2018) 20906–20912. <https://doi.org/10.1016/j.ceramint.2018.08.097>.
- 760 [43] V.I. Popkov, O. V. Almjasheva, M.P. Schmidt, S.G. Izotova, V. V. Gusarov, Features  
761 of nanosized YFeO<sub>3</sub> formation under heat treatment of glycine-nitrate combustion products,  
762 *Russ. J. Inorg. Chem.* 60 (2015) 1193–1198. <https://doi.org/10.1134/S0036023615100162>.
- 763 [44] K.D. Martinson, I.B. Pantelev, A.P. Shevchik, V.I. Popkov, Effect of the Red/ox ratio  
764 on the structure and magnetic behavior of Li<sub>0.5</sub>Fe<sub>2.5</sub>O<sub>4</sub> nanocrystals synthesized by solution  
765 combustion approach, *Lett. Mater.* 9 (2019) 475–479. [https://doi.org/10.22226/2410-3535-](https://doi.org/10.22226/2410-3535-2019-4-475-479)  
766 [2019-4-475-479](https://doi.org/10.22226/2410-3535-2019-4-475-479).
- 767 [45] N.A. Lomanova, M. V. Tomkovich, D.P. Danilovich, A. V. Osipov, V. V. Panchuk,  
768 V.G. Semenov, I. V. Pleshakov, M.P. Volkov, V. V. Gusarov, Magnetic Characteristics of  
769 Nanocrystalline BiFeO<sub>3</sub>-Based Materials Prepared by Solution Combustion Synthesis, *Inorg.*  
770 *Mater.* 56 (2020) 1271–1277. <https://doi.org/10.1134/S0020168520120110/FIGURES/5>.
- 771 [46] N.A. Lomanova, V. V. Panchuk, V.G. Semenov, I. V. Pleshakov, M.P. Volkov, V. V.  
772 Gusarov, Bismuth orthoferrite nanocrystals: magnetic characteristics and size effects,  
773 *Ferroelectrics.* 569 (2020) 240–250. <https://doi.org/10.1080/00150193.2020.1822683>.



- 774 [47] H. Maleki, M. Zakeri, R. Fathi, Experimental study of the effect of yttrium on the  
775 structural, thermal, and magnetic properties of BiFeO<sub>3</sub>, *Appl. Phys. A Mater. Sci. Process.* 124  
776 (2018) 1–6. <https://doi.org/10.1007/S00339-018-2154-8/TABLES/1>.
- 777 [48] N.I. Ilić, J.D. Bobić, B.S. Stojadinović, A.S. Džunuzović, M.M. Vijatović Petrović,  
778 Z.D. Dohčević-Mitrović, B.D. Stojanović, Improving of the electrical and magnetic properties  
779 of BiFeO<sub>3</sub> by doping with yttrium, *Mater. Res. Bull.* 77 (2016) 60–69.  
780 <https://doi.org/10.1016/J.MATERRESBULL.2016.01.018>.
- 781 [49] Z.A. Samoilenko, N.N. Ivakhnenko, E.I. Pushenko, V.Y. Sycheva, N.A. Ledenev, A.  
782 V. Pashchenko, The Influence of the Composition on the Atomic Structure of Bi<sub>1-x</sub>Y<sub>x</sub>FeO<sub>3</sub>  
783 Ceramics, *Tech. Phys.* 66 (2021) 793–797.  
784 <https://doi.org/10.1134/S1063784221050212/FIGURES/6>.
- 785 [50] A. Perejón, E. Gil-González, P.E. Sánchez-Jiménez, J.M. Criado, L.A. Pérez-Maqueda,  
786 Structural, Optical, and Electrical Characterization of Yttrium-Substituted BiFeO<sub>3</sub> Ceramics  
787 Prepared by Mechanical Activation, *Inorg. Chem.* 54 (2015) 9876–9884.  
788 <https://doi.org/10.1021/ACS.INORGCHEM.5B01654>.
- 789 [51] Z. Li, L. Cheng, K. Zhang, Z. Wang, Enhanced photocatalytic performance by Y-doped  
790 BiFeO<sub>3</sub> particles derived from MOFs precursor based on band gap reduction and oxygen  
791 vacancies, *Appl. Organomet. Chem.* 35 (2021). <https://doi.org/10.1002/AOC.6113>.
- 792 [52] V. Runco Leal, C. Navarro, G. Bridoux, M. Villafuerte, M.I. Gómez, Preparation and  
793 characterization of a new series of solid solutions of Bi<sub>1-x</sub>Y<sub>x</sub>FeO<sub>3</sub> (0 < x < 1) from the thermal  
794 decomposition of hexacyanoferrates doped with yttrium, *J. Therm. Anal. Calorim.* 135 (2019)  
795 3259–3268. <https://doi.org/10.1007/S10973-018-7593-0/FIGURES/11>.
- 796 [53] R.D. Shannon, Revised effective ionic radii and systematic studies of interatomic  
797 distances in halides and chalcogenides, *Acta Crystallogr. Sect. A.* 32 (1976) 751–767.  
798 <https://doi.org/10.1107/S0567739476001551>.
- 799 [54] N.S. Parvathy, R. Govindaraj, Atomic scale insights on the growth of BiFeO<sub>3</sub>  
800 nanoparticles, *Sci. Rep.* 12 (2022) 1–17. <https://doi.org/10.1038/S41598-022-08687->  
801 [1](https://doi.org/10.1038/S41598-022-08687-1);SUBJMETA.
- 802 [55] A. Jakimińska, M. Pawlicki, W. Macyk, Photocatalytic transformation of Rhodamine  
803 B to Rhodamine-110 – The mechanism revisited, *J. Photochem. Photobiol. A Chem.* 433  
804 (2022) 114176. <https://doi.org/10.1016/J.JPHOTOCHEM.2022.114176>.
- 805 [56] I.K. Konstantinou, T.A. Albanis, TiO<sub>2</sub>-assisted photocatalytic degradation of azo dyes  
806 in aqueous solution: kinetic and mechanistic investigations: A review, *Appl. Catal. B Environ.*  
807 49 (2004) 1–14. <https://doi.org/10.1016/J.APCATB.2003.11.010>.



- 808 [57] S.M. Tikhanova, M.I. Tenevich, A.N. Matveyeva, M.O. Enikeeva, A.D. Trofimuk, View Article Online  
DOI: 10.1039/D6MA00153J
- 809 V.N. Nevedomskiy, S.E. Yu, D.S. Dmitriev, V.I. Popkov, Solution combustion synthesis of
- 810 phase-pure, foam-like hexagonal LuFeO<sub>3</sub>: visible-light photocatalyst with high activity, Appl.
- 811 Surf. Sci. 729 (2026). <https://doi.org/10.1016/j.apsusc.2026.166181>.



## Data Availability Statement

- No primary research results, software or code have been included and no new data were generated or analysed as part of this review.

View Article Online  
DOI: 10.1039/D6MA00153J

